

Notice: This manuscript has been authored by UT-Battelle, LLC, under Contract No. DE-AC0500OR22725 with the U.S. Department of Energy. The United States Government retains and the publisher, by accepting the article for publication, acknowledges that the United States Government retains a non-exclusive, paid-up, irrevocable, world-wide license to publish or reproduce the published form of this manuscript, or allow others to do so, for the United States Government purposes. The Department of Energy will provide public access to these results of federally sponsored research in accordance with the DOE Public Access Plan (<http://energy.gov/downloads/doe-public-access-plan>).

# Dissolution and Initial Hydration Behavior of Tricalcium Aluminate in Low Activity Sulfate Solutions

Alexander S. Brand<sup>1,2\*</sup>, Steven B. Feldman<sup>2</sup>, Paul E. Stutzman<sup>2</sup>, Anton V. Ievlev<sup>3</sup>, Matthias Lorenz<sup>3</sup>, Darren C. Pagan<sup>4</sup>, Sriramy Nair<sup>4</sup>, Justin M. Gorham<sup>5</sup>, and Jeffrey W. Bullard<sup>2</sup>

<sup>1</sup> Department of Civil and Environmental Engineering, Virginia Polytechnic Institute and State University, Blacksburg, VA, USA, 24061

<sup>2</sup> Materials and Structural Systems Division, Engineering Laboratory, National Institute of Standards and Technology, Gaithersburg, MD, USA, 20877

<sup>3</sup> Center for Nanophase Materials Sciences, Oak Ridge National Laboratory, Oak Ridge, TN, USA, 37831

<sup>4</sup> Cornell High Energy Synchrotron Source, Cornell University, Ithaca, NY, USA, 14853

<sup>5</sup> Materials Measurement Science Division, Materials Measurement Laboratory, National Institute of Standards and Technology, Gaithersburg, MD, USA, 20877

\* Corresponding author: [asbrand@vt.edu](mailto:asbrand@vt.edu)

## Abstract

Influences of alkali or alkaline earth sulfates on the hydration of cubic tricalcium aluminate ( $C_3A$ ) were evaluated by *in situ* dissolution rate measurements, by *ex situ* near-surface composition measurements with secondary ion mass spectrometry, and by *in situ* synchrotron X-ray diffraction to monitor precipitation of hydration products. Both slight reductions in dissolution rate and cation-specific interactions with the solid were observed. The near-surface Ca/Al ratio is significantly lower after some dissolution, and the electrolyte cations are incorporated within the surface with different affinities ( $Mg^{2+} > K^+ > Na^+$ ). An interfacial dissolution-precipitation mechanism may explain the observations as well as, or better than, a simple cation exchange. The sulfate concentration in solution affects the rates of both  $C_3A$  dissolution and precipitation of hydration products. Sulfate ions likely adsorb at the hydrous aluminum-rich surface layer, thereby reducing the dissolution rate of aluminates and delaying the precipitation of aluminate hydration products.

*Keywords:* Kinetics (A),  $Ca_3Al_2O_6$  (D), X-Ray Diffraction (B), Hydration (A), Dissolution

## 1. INTRODUCTION

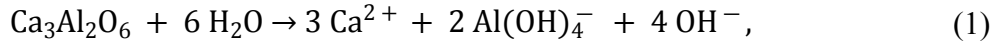
Tricalcium aluminate ( $Ca_3Al_2O_6$  or  $C_3A^*$ ) is a principal component in portland cement clinker, accounting for up to 10 % of the composition by mass [1]. Its reaction with water is extremely rapid and generates large calcium aluminate hydrate crystals that are responsible for flash setting of cement [1]. The rates of these reactions in portland cement can be regulated by mixing or intergrinding the clinker with gypsum or other soluble calcium sulfate minerals. Understanding the interaction of  $C_3A$  with dissolved sulfate salts, and how those interactions affect the initial dissolution of  $C_3A$ , is therefore important for controlling early-age hydration and microstructure development in cementitious composites. Prior studies suggest that  $C_3A$  reactivity is diminished by sulfate ion adsorption at  $C_3A$  defect sites [2–7] or by sulfate and calcium ion adsorption on an aluminum-rich surface layer [8–11], and the current study seeks to build on

---

\* By conventional cement chemistry notation: C=CaO, A= $Al_2O_3$ , S= $SiO_2$ , F= $Fe_2O_3$ , H= $H_2O$ ,  $\bar{S}$ = $SO_3$  [1]

those studies by providing more knowledge about the implications for phase evolution and kinetics.

A recent investigation of C<sub>3</sub>A polycrystals in water has shown that the dissolution rate varies considerably across the surface and is correlated with different defect regions at the surface such as etch pits and grain boundaries [12]. This behavior is consistent with prior observations on a wide range of minerals [13–26], including cementitious minerals [12, 27–29], resulting in the interpretation of dissolution rates as a probability distribution or so-termed “rate spectrum.” Measuring how partially saturated sulfate salt solutions alter the rate and its variability, relative to dissolution in pure water, may provide insights about the role of sulfates in regulating C<sub>3</sub>A hydration reactions. Based on the net reaction for dissociation of C<sub>3</sub>A in water,



the rate of the forward reaction ( $J_+$ ) is expected to depend primarily on the water activity and the surface concentration of reactive sites [12], while the reverse reaction flux ( $J_-$ ) is expected to depend primarily on the activities of the dissolved components. The net dissolution flux ( $J_{\text{net}}$ ) is assumed to have the generic form

$$J_{\text{net}} = J_+ - J_- = k_+ (a_{\text{H}_2\text{O}})^n - k_- (a_{\text{Ca}^{2+}})^{m_1} (a_{\text{Al}(\text{OH})_4^-})^{m_2} (a_{\text{OH}^-})^{m_3}, \quad (2)$$

where  $a$  is the activity of each of the species,  $k_+$  and  $k_-$  are the apparent forward and reverse reaction rate coefficients, respectively, and  $n$ ,  $m_1$ ,  $m_2$ , and  $m_3$  are empirical reaction order constants. The previous study by Brand and Bullard [12] experimentally measured the statistical distribution of  $k_+$  as having a median of  $2.1 \mu\text{mol m}^{-2} \text{s}^{-1}$  at a constant  $n = 5.2$  for the same cubic C<sub>3</sub>A powder used in this study.

Sulfate salt solutions can, in principle, affect the apparent rate constants through their effects on ionic strength, surface adsorption, and the composition and thickness of the electrical double layer. Previous studies have shown that calcium sulfate initially delays the hydration of C<sub>3</sub>A (*e.g.*, [2,27]), that magnesium sulfate may increase the C<sub>3</sub>A hydration rate [28], and that sodium sulfate does not appreciably affect C<sub>3</sub>A hydration [29,30]. This suggests some cation-specific effects on dissolution that require further investigation. The present study builds upon those studies by examining how solutions of Na<sub>2</sub>SO<sub>4</sub>, K<sub>2</sub>SO<sub>4</sub>, or MgSO<sub>4</sub> modify the near-surface composition of C<sub>3</sub>A, how they alter the rate and variability of C<sub>3</sub>A dissolution, and how they influence the timing and rate of precipitation of solid hydration products at early reaction times.

## 2. EXPERIMENTAL METHODS

Cubic C<sub>3</sub>A was obtained from Mineral Research Processing (Mezyrieu, France).<sup>†</sup> The C<sub>3</sub>A mineral samples were crushed and micronized in ethanol prior to experimentation. The chemical composition, determined by inductively coupled plasma optical emission spectroscopy (ICP-OES) on acid-digested samples, is  $(64.6 \pm 1.2) \%$  CaO and  $(35.4 \pm 0.6) \%$  Al<sub>2</sub>O<sub>3</sub> by mass [12], corresponding to a molar Ca/Al ratio of  $1.66 \pm 0.04$ . X-ray powder diffraction (XRD), using Cu K $\alpha$  radiation and 50 % rutile as an internal standard, indicated that the solid was, by mass, (89.7

---

<sup>†</sup> Certain commercial equipment, instruments, or materials are identified in this paper to foster understanding. Such identification does not imply recommendation or endorsement by the National Institute of Standards and Technology, nor does it imply that the materials or equipment identified are necessarily the best available for the purpose.

$\pm 0.5$ ) % cubic  $C_3A$ , ( $2.2 \pm 0.1$ ) % free lime, ( $4.3 \pm 0.2$ ) % mayenite ( $C_{12}A_7$ ), and ( $3.8 \pm 0.6$ ) % amorphous content [12]. The particle size distribution, measured by laser diffraction, is shown in Figure 1. The 10<sup>th</sup>, 50<sup>th</sup>, and 90<sup>th</sup> percentile particle sizes are 1.1  $\mu m$ , 3.8  $\mu m$ , and 9.4  $\mu m$ , respectively.

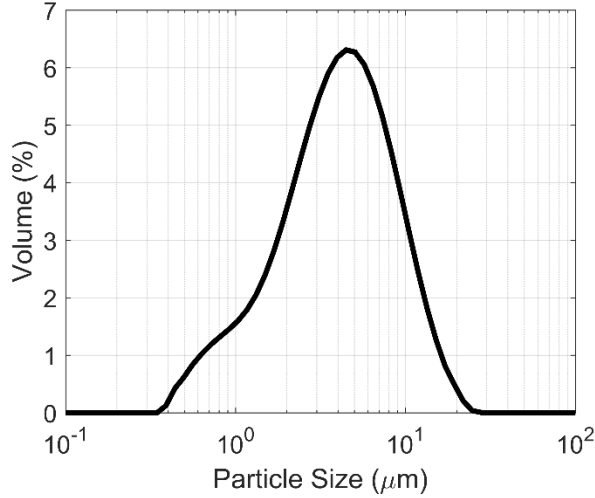


Figure 1. Cumulative particle size distribution for micronized  $C_3A$ .

## 2.1 Dissolution

In situ digital holographic microscopy (DHM) in reflection mode was used to track the real-time nanoscale changes in surface topography of  $C_3A$  polycrystals. Sample preparation and data analysis for DHM follow the procedures described previously for  $C_3A$  [12], with additional details presented elsewhere [18,24,25,31]. A sintered, polished  $C_3A$  specimen was bonded to a titanium stub that was locked into a chemically inert flow-through reaction cell. A  $20\times$  immersion lens was used for all experiments. Once every 10 s to 30 s, a set of 15 to 20 holograms was collected at a rate of  $12.5\text{ s}^{-1}$ . Each set was averaged to be representative of the corresponding time interval to reduce the noise [31]. The temperature of the solution at the inlet was ( $23 \pm 1$ )  $^{\circ}C$ . As determined by prior study [12], a volumetric flow rate of ( $33 \pm 0.5$ )  $mL\text{ min}^{-1}$  was used to ensure that dissolution was controlled primarily by surface reaction rather than transport of dissolved ions away from the boundary layer. The baseline uncertainty in surface height for this experimental configuration, characterized as the temporal standard deviation per pixel for a flat glass surface undergoing no dissolution, has been determined to be 0.41 nm [31].

$C_3A$  surfaces undergo small-scale roughening in water so rapidly that the reflected DHM signal is lost due to diffuse scattering in less than a minute and holograms cannot be collected. The rate of dissolution and roughening was reduced by diluting deionized water ( $> 0.18\text{ M}\Omega\text{ m}$ ) with absolute ethanol at a mole fraction of 0.317 [12].

Surface normal dissolution velocities,  $v_s$  ( $m\text{ s}^{-1}$ ), are measured by dividing the height change by time,  $\Delta h/\Delta t$ , at each pixel in the DHM image. The surface normal rate,  $J_s$  ( $mol\text{ m}^{-2}\text{ s}^{-1}$ ), is proportional to the normal velocity [32,33],

$$J_s = \frac{v_s}{V_m} = \frac{\Delta h}{\Delta t V_m}, \quad (3)$$

where the molar volume of  $C_3A$ ,  $V_m$  ( $m^3 \text{ mol}^{-1}$ ), is assumed to be  $8.91 \times 10^{-5} \text{ m}^3 \text{ mol}^{-1}$  [34]. By convention, positive values of  $v_s$  and  $J_s$  will be considered dissolution.

Studying the influence of calcium sulfate on  $C_3A$  dissolution is desirable because of the widespread use of calcium sulfate to regulate  $C_3A$  and  $C_4AF$  hydration in portland cement [3,6]. However, calcium sulfate is insoluble in the water-ethanol mixtures used for the DHM measurements. Therefore, three other soluble sulfate salts were evaluated: magnesium sulfate ( $MgSO_4$ ), potassium sulfate ( $K_2SO_4$ ), and sodium sulfate ( $Na_2SO_4$ ). All three salts dissolve readily in the water-ethanol mixture used here. Omitting calcium sulfate from this part of the study also avoids the direct influence it would have on the saturation state with respect to  $C_3A$ . Sulfate solutions with each of these three salts were formulated at different concentrations to isolate the influence of cations and sulfate anions. Experiments using  $MgSO_4$ , the most soluble of the three salts, were conducted at concentrations of  $1 \text{ mmol L}^{-1}$ ,  $2.5 \text{ mmol L}^{-1}$ ,  $5 \text{ mmol L}^{-1}$ ,  $10 \text{ mmol L}^{-1}$ , and  $15 \text{ mmol L}^{-1}$ .<sup>‡</sup> Because of their lower solubility, both  $Na_2SO_4$  and  $K_2SO_4$  were examined only at concentrations of  $0.5 \text{ mmol L}^{-1}$  and  $1 \text{ mmol L}^{-1}$ .

Some of the  $C_3A$  samples were examined after the dissolution measurements by scanning electron microscopy (SEM) and energy dispersive X-ray spectroscopy (EDXS). The samples were coated with carbon prior to examination by SEM.

## 2.2 Surface Composition

The  $C_3A$  surface before and after exposure to a water-ethanol solution without any sulfates was first examined by X-ray photoelectron spectroscopy (XPS). An Axis Ultra DLD (Kratos Analytical, Chestnut Ridge, NY) was used in a high-vacuum system maintained at  $0.27 \mu\text{Pa}$  ( $2 \times 10^{-9}$  Torr). Photoemission was achieved using monochromatic Al  $K\alpha$  X-rays (150 W) at an incidence angle of 60 degrees from surface normal. Photoelectrons were collected along the surface normal from an approximately  $190 \mu\text{m}$  diameter spot. Photoelectrons were separated using a hemispherical analyzer at a pass energy of 40 eV in 0.1 eV steps. Collected spectra were processed using commercially available software (CasaXPS, Teignmouth, UK) and elemental areas were corrected using elemental relative sensitivity factors provided by the manufacturer. Data were collected from each specimen at three or five different regions on the surface. O 1s, Ca 2p, C 1s and Al 2p were observed in all specimens while S 2p, Si 2p and Mg 2p were observed in the specimen exposed to water-ethanol solution. Next, sputtering using 4 kV argon ions for 30 s was performed on the same specimens to remove surface contamination, including from some adventitious carbon contamination caused by exposure to air and from any ethanol, magnesium, or sulfur adsorption from the solution, while attempting to minimize surface mixing and preferential sputtering. After sputtering, an additional three measurements were made on each of the surfaces.

Samples after the DHM experimentation with and without  $1 \text{ mmol L}^{-1}$  sulfate solution were also examined for near-surface chemical composition using high resolution focused ion beam time-of-flight secondary ion mass spectrometer (FIB/TOF-SIMS). Specifically, a TOF.SIMS 5 (IONTOF, Munster, Germany) instrument was utilized at the Center for Nanophase Materials Sciences at Oak Ridge National Laboratory. A  $Bi_3^+$  ion beam with a 30 keV projectile

---

<sup>‡</sup> Concentration uncertainties are  $0.02 \text{ mmol L}^{-1}$ ,  $0.03 \text{ mmol L}^{-1}$ , and  $0.04 \text{ mmol L}^{-1}$  for  $MgSO_4$ ,  $K_2SO_4$ , and  $Na_2SO_4$ , respectively.

energy, a current of 0.5 nA, and a ~100 nm spot size was used as a primary ion source to create secondary ions of the analyte. Extracted ions were analyzed using a time-of-flight mass analyzer in positive ion detection mode with a mass resolution  $m/\Delta m$  of 3000 to 10,000. A  $\text{Cs}^+$  ion beam with 1 keV projectile energy, current of ~25 nA, and ~20  $\mu\text{m}$  spot size was used for depth profiling. The dual-beam experiment was performed in non-interlaced mode using cycles of four analysis frames and 10 s sputter erosion with charge compensation enabled. The analysis beam scanned a field of view of 100  $\mu\text{m}$  by 100  $\mu\text{m}$  with 256 pixels by 256 pixels in a random scan pattern; the sputter beam was set to erode a crater with 400  $\mu\text{m}$  by 400  $\mu\text{m}$  dimensions. This instrument was also equipped with atomic force microscopy (AFM) in the same vacuum chamber (TOF.SIMS NCS) to assess the depth of chemical profiling. For this purpose, AFM line scans of 750  $\mu\text{m}$  length were recorded to profile sputter craters of identical dimensions after different total sputter times.

### 2.3 *In situ* XRD

The reaction of  $\text{C}_3\text{A}$  with water is so rapid that the first hydration products have been observed to form within the first tens of seconds after contact with water [35,36]. One powerful technique to study reactions on such a time scale is synchrotron radiation X-ray diffraction (SRXRD) [37,38], as has been demonstrated by various *in situ* hydration studies of  $\text{C}_3\text{A}$  [35,36,39–41]. The effects of different sulfate salts on the initial hydration of  $\text{C}_3\text{A}$  were monitored by *in situ* SRXRD at Beamline F2 at the Cornell High Energy Synchrotron Source (CHESS). The incident hard X-ray radiation was 41.991 keV (29.526 pm wavelength). The diffraction pattern was captured on a two-dimensional (2D) area detector located about 315 mm from the sample. Calibration was performed with a ceria ( $\text{CeO}_2$ ) standard. 2D diffraction patterns were collected once every second, enabling the detection of the first reaction products near the moment when they form. The X-ray beam covered a 1.0 mm strip over the full width of the sample. The 2D data were processed with HEXRD [42] to produce 1D diffraction patterns of intensity plotted against  $2\theta$  diffraction angle. Using GSAS-II [43], a Chebyshev polynomial was fit to the background of each dataset at the start of the experiment, which was then assumed to remain constant and subtracted from the patterns at every time step. Phase identifications were made using the following Powder Diffraction Files (PDF): PDF 38-1429 (cubic  $\text{C}_3\text{A}$ ) [44], PDF 1-83-1289 (sulfate AFm) [45], PDF 42-487 (hydroxy AFm) [46], and PDF 24-217 (hydrogarnet) [47]. The hemicarboaluminate and ettringite structures by Runčevski *et al.* [48] and Goetz-Neunhoeffler and Neubauer [49], respectively, were also utilized.

To capture *in situ* hydration behavior, a remotely controlled syringe pump was used to inject a known solution volume into a  $\text{C}_3\text{A}$  powder bed confined in a glass capillary tube (see Appendix, Figure A.1). A 1.0 mL glass syringe was used, and the solution was injected at a rate of 0.85 mL  $\text{min}^{-1}$ , which was the fastest rate that the pump could output for the size of syringe used. The pump volumetric dispensing accuracy reported by the manufacturer is  $\pm 1\%$ .

After several trials with glass capillary sizes and liquid-to-powder ratios, a 1.5 mm diameter tube (10  $\mu\text{m}$  wall thickness) and a liquid-to-powder mass ratio of 1.0 were chosen to provide the best control over solution injection by minimizing the capillary forces. Wetting of the entire powder mass was achieved by inserting glass wool into the capillary tube and then adding 15 mg to 20 mg of powder on top of the wool pack (see Appendix, Figure A.2). The X-

ray beam was centered on the upper section of powder that would be first wetted by the injected solution. Gentle external vibration was also applied to significantly improve wetting of the entire powder bed.

*In situ* hydration experiments were conducted with 10 mmol L<sup>-1</sup> solutions of reagent grade ( $\geq 99$  % by mass) CaSO<sub>4</sub>, MgSO<sub>4</sub>, K<sub>2</sub>SO<sub>4</sub>, or Na<sub>2</sub>SO<sub>4</sub> along with deionized water. Ethanol dilution was not used because SRXRD measurements are not sensitive to rates of surface roughening. At least two replicates were tested for each solution.

### 3. RESULTS

#### 3.1 Dissolution Experiments

##### 3.1.1. Effect of MgSO<sub>4</sub> Concentration

As expected from previous C<sub>3</sub>A dissolution experiments [12], the dissolution rate has a skewed distribution with or without MgSO<sub>4</sub> (Figure 2). Increasing the MgSO<sub>4</sub> concentration shifts the distribution to lower rates (Figure 2 and Table 1). The effect increases with MgSO<sub>4</sub> concentration up to about 2.5 mmol L<sup>-1</sup>, above which the median rate and interquartile range of the distribution are approximately independent of concentration (Figure 3).

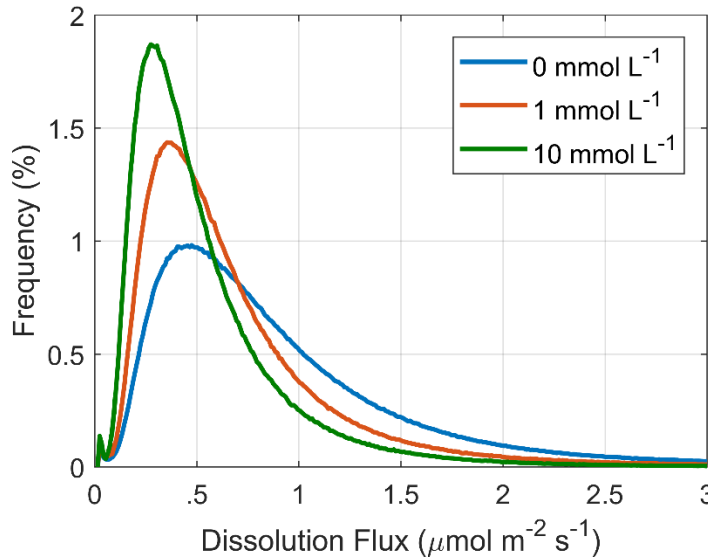


Figure 2. Dissolution rate distribution of C<sub>3</sub>A exposed to flowing MgSO<sub>4</sub> solutions at concentrations of 0 mmol L<sup>-1</sup>, 1 mmol L<sup>-1</sup>, and 10 mmol L<sup>-1</sup>.

Table 1. Dependence of C<sub>3</sub>A Dissolution Rate Statistics on MgSO<sub>4</sub> Concentration\*

Solution [SO <sub>4</sub> <sup>2-</sup> ] (mmol L <sup>-1</sup> )	Dissolution Flux (μmol m <sup>-2</sup> s <sup>-1</sup> )				Number of Data Points
	Mean	Median	Standard Deviation	IQR (P <sub>25</sub> ,P <sub>75</sub> )**	
0	1.121	0.754	1.57	0.741 (0.473,1.214)	10 <sup>6.91</sup>
1	0.736	0.553	0.752	0.494 (0.364,0.858)	10 <sup>6.68</sup>
2.5	0.559	0.446	0.451	0.367 (0.303,0.670)	10 <sup>6.45</sup>
5	0.627	0.471	0.628	0.464 (0.290,0.754)	10 <sup>6.55</sup>
10	0.548	0.429	0.453	0.383 (0.283,0.666)	10 <sup>6.64</sup>
15	0.621	0.508	0.430	0.466 (0.337,0.767)	10 <sup>6.51</sup>

\* All solutions used a water-ethanol solvent with ethanol mole fraction of 0.317

\*\*The 25<sup>th</sup> (P<sub>25</sub>) and 75<sup>th</sup> (P<sub>75</sub>) percentiles that correspond to the IQR

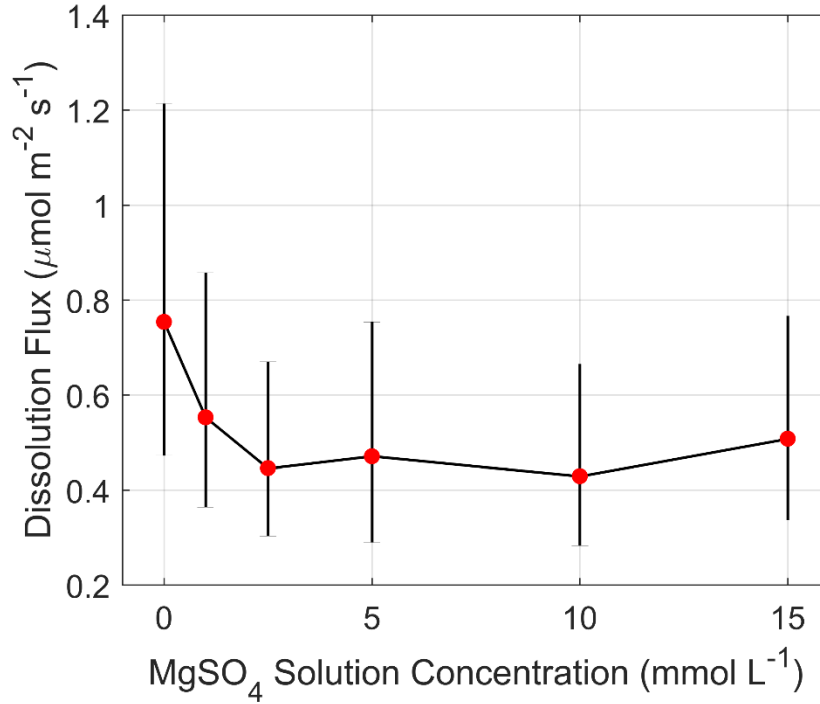


Figure 3. Median dissolution flux (red circles) as a function of MgSO<sub>4</sub> concentration. The bars indicate the IQRs given in Table 1.

### 3.1.2 Cation-Specific Effects: Constant Sulfate Concentration

1 mmol L<sup>-1</sup> of each of the sulfate salts was used to evaluate the effect of different cations at constant sulfate concentration (Figure 4a). Table 2 shows the characteristics of the dissolution flux distributions and suggests that there may be a cationic effect on dissolution rates even though the sulfate concentration is constant. While all three sulfate salts reduce the C<sub>3</sub>A dissolution flux, K<sub>2</sub>SO<sub>4</sub> has a modestly greater retarding effect than either MgSO<sub>4</sub> or Na<sub>2</sub>SO<sub>4</sub>.

Table 2. C<sub>3</sub>A Dissolution Rates at Constant Sulfate Concentration

Cation	Solution			Dissolution Flux (μmol m <sup>-2</sup> s <sup>-1</sup> )				Number of Data Points
	[Sulfate] (mmol L <sup>-1</sup> )	[Cation] (mmol L <sup>-1</sup> )	Ionic Strength (mmol L <sup>-1</sup> )	Mean	Median	Standard Deviation	IQR (P <sub>25</sub> , P <sub>75</sub> )*	
None	0	0	0	1.121	0.754	1.57	0.741 (0.473, 1.214)	10 <sup>6.91</sup>
Mg <sup>2+</sup>	1	1	4	0.736	0.553	0.752	0.494 (0.364, 0.858)	10 <sup>6.68</sup>
K <sup>+</sup>	1	2	3	0.621	0.445	0.866	0.391 (0.295, 0.686)	10 <sup>6.95</sup>
Na <sup>+</sup>	1	2	3	0.925	0.585	1.55	0.580 (0.377, 0.957)	10 <sup>6.28</sup>

\*The 25<sup>th</sup> (P<sub>25</sub>) and 75<sup>th</sup> (P<sub>75</sub>) percentiles that correspond to the IQR

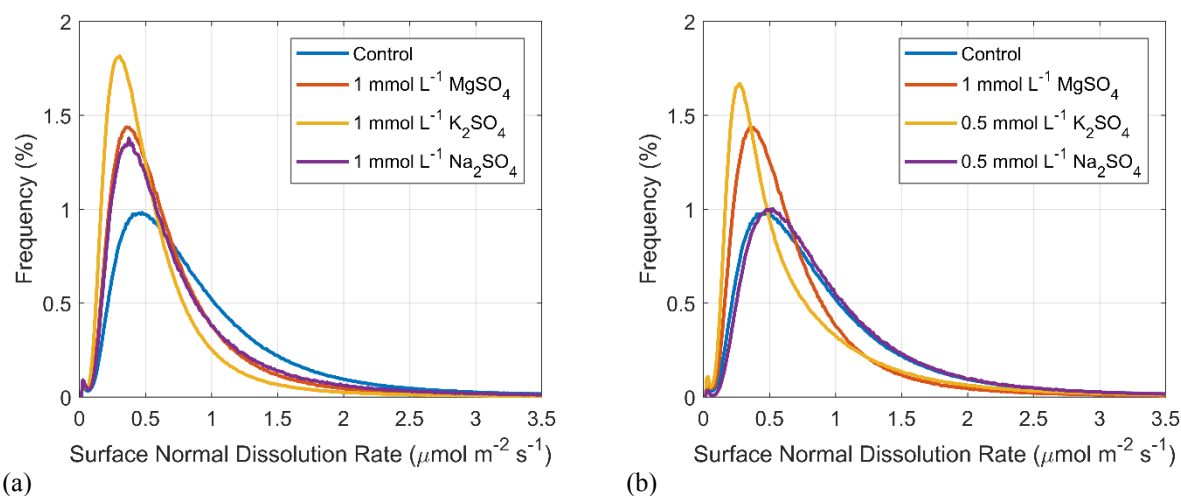


Figure 4. Cationic effects on  $C_3A$  dissolution in the presence of sulfate: (a) constant sulfate concentration and (b) constant cation concentration.

### 3.1.3 Cation-Specific Effects: Constant Cation Concentration

Experiments performed at a constant cation concentration of  $1 \text{ mmol L}^{-1}$  were otherwise identical to those described in Section 3.1.2. Figure 4b shows how the cation influences the dissolution rate distributions, and the characteristics of those distributions are given in Table 3. The cation type influences the median dissolution flux by up to 35 % at equal concentrations.  $\text{Na}_2\text{SO}_4$  has the least effect on  $C_3A$  dissolution; in fact, the dissolution rates in  $0.5 \text{ mmol L}^{-1}$   $\text{Na}_2\text{SO}_4$  are about the same as those in pure water. In contrast, solutions with  $\text{Mg}^{2+}$  and  $\text{K}^+$  at equal concentrations both reduce the dissolution rates by comparable degrees despite their different sulfate ion concentrations and ionic strengths.

Table 3.  $C_3A$  Dissolution Rates at Constant Cation Concentration

Cation	Solution			Dissolution Flux ( $\mu\text{mol m}^{-2} \text{ s}^{-1}$ )				Number of Data Points
	[Sulfate] ( $\text{mmol L}^{-1}$ )	[Cation] ( $\text{mmol L}^{-1}$ )	Ionic Strength ( $\text{mmol L}^{-1}$ )	Mean	Median	Standard Deviation	IQR ( $P_{25}, P_{75}$ )*	
None	0	0	0	1.121	0.754	1.57	0.741 (0.473, 1.214)	$10^{6.91}$
$\text{Mg}^{2+}$	1	1	4	0.736	0.553	0.752	0.494 (0.364, 0.858)	$10^{6.68}$
$\text{K}^+$	0.5	1	1.5	0.821	0.497	1.21	0.611 (0.302, 0.913)	$10^{6.92}$
$\text{Na}^+$	0.5	1	1.5	1.108	0.781	1.39	0.725 (0.506, 1.231)	$10^{6.48}$

\*The 25<sup>th</sup> ( $P_{25}$ ) and 75<sup>th</sup> ( $P_{75}$ ) percentiles that correspond to the IQR

### 3.1.4 SEM and EDXS of $C_3A$ Surfaces after Dissolution

The  $C_3A$  surface after exposure to flowing  $\text{MgSO}_4$  solution (Figure 5a) is not as rough as it is after dissolution in water-ethanol mixtures (*e.g.*, see Ref. [12]). Ettringite needles were observed only when using the most concentrated  $\text{MgSO}_4$  solution,  $15 \text{ mmol L}^{-1}$  (Figure 5b),

although those ettringite crystals may have formed after the experiment while the sample was being removed due to evaporation of a fluid film present on the surface. No ettringite or other precipitated phases were observed by SEM after exposure to any of the other solutions, including those with lower  $\text{MgSO}_4$  concentrations.

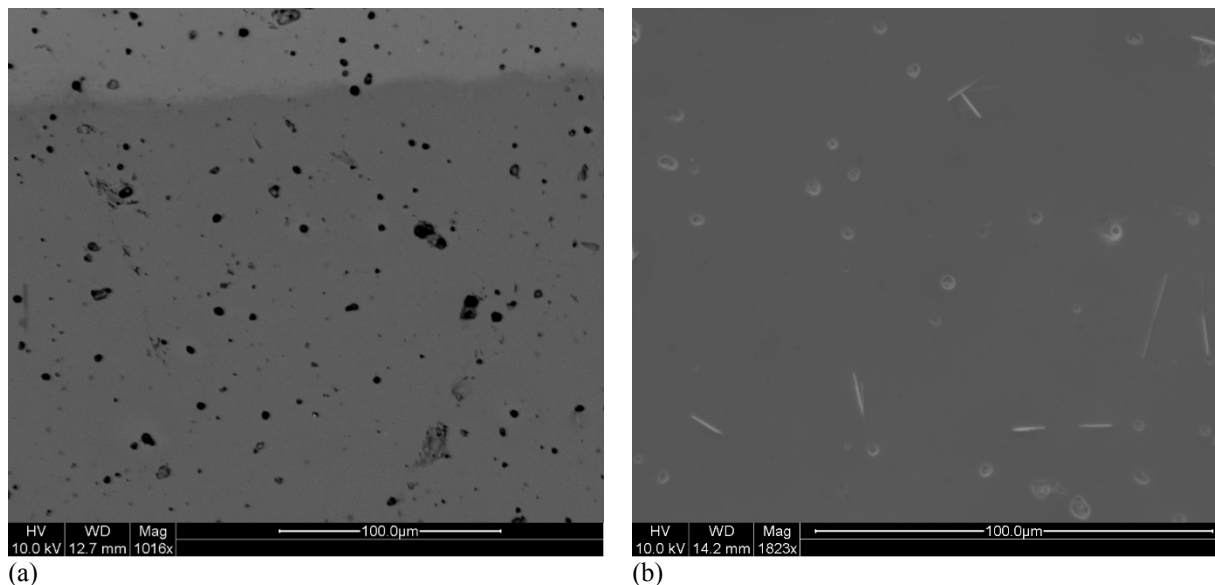


Figure 5. (a) BSE image of  $\text{C}_3\text{A}$  surface after 35 min exposure to flowing  $10 \text{ mmol L}^{-1}$   $\text{MgSO}_4$  solution and (b) secondary electron image of  $\text{C}_3\text{A}$  surface after 40 min exposure to flowing  $15 \text{ mmol L}^{-1}$   $\text{MgSO}_4$  solution.

Chemical compositions of  $\text{C}_3\text{A}$  surfaces exposed to solutions with and without sulfates were inferred from EDXS spectra collected at no fewer than 200 points. The compositions are given as molar ratios in Table 4. Stoichiometric  $\text{C}_3\text{A}$  has a Ca/Al ratio of 1.5. However, the Ca/Al ratio inferred from EDXS analysis is about 1.7, close to the bulk Ca/Al ratio of  $1.66 \pm 0.04$  measured on the digested  $\text{C}_3\text{A}$  powder by ICP-OES (Section 2). Dissolution in flowing  $\text{MgSO}_4$  solutions is accompanied by a significant decrease in Ca/Al as well as small proportion of residual Mg in the surface layer afterward (Table 4). The observed Mg/Ca ratio of 0.03 is significant, especially considering that it is averaged over the EDXS interaction depth, which suggests either a concentrated adsorbed layer of Mg or a partial substitution of  $\text{Mg}^{2+}$  for  $\text{Ca}^{2+}$  in the  $\text{C}_3\text{A}$  crystal structure even though the  $\text{Mg}^{2+}$  ion is 30 % smaller than  $\text{Ca}^{2+}$  (*i.e.*, the effective ionic radii for  $\text{Ca}^{2+}$  and  $\text{Mg}^{2+}$  are 100 pm and 72 pm [50], respectively). The (Ca+Mg)/Al ratio is  $1.620 \pm 0.052$ , so the  $\text{MgSO}_4$  solutions still cause some net loss of cations relative to aluminates in the dissolving surface layer even if some substitution is occurring. In contrast, neither of the alkali solutions caused a significant change in Ca/Al averaged over the  $\approx 2 \mu\text{m}$  interaction depth probed by EDXS, nor were any residual alkali measured on the solid after exposure to those solutions. Finally, all of the sulfate solutions leave behind a small but detectable concentration of sulfur at the surface.

Table 4. Mean Atomic Ratios from EDXS Point Count Analysis\*

Experimental Condition	Solution	Ca/Al	(Mg, Na, or K)/Ca	S/Ca	No. of Points
No Sulfate	Unreacted	1.741(50)	0	0	506
	Water-ethanol	1.733(56)	0	0	249
Constant Sulfate	MgSO <sub>4</sub> (1 mmol L <sup>-1</sup> )	1.567(53)	0.034(4)	0.008(1)	256
	K <sub>2</sub> SO <sub>4</sub> (1 mmol L <sup>-1</sup> )	1.754(43)	0	0.005(1)	250
	Na <sub>2</sub> SO <sub>4</sub> (1 mmol L <sup>-1</sup> )	1.706(47)	0	0.007(2)	250
Constant Cation	MgSO <sub>4</sub> (1 mmol L <sup>-1</sup> )	1.567(53)	0.034(4)	0.008(1)	256
	K <sub>2</sub> SO <sub>4</sub> (0.5 mmol L <sup>-1</sup> )	1.727(41)	0	0.007(2)	250
	Na <sub>2</sub> SO <sub>4</sub> (0.5 mmol L <sup>-1</sup> )	1.762(42)	0	0.005(1)	253

\*Values in parentheses are the uncertainties in the most significant digits characterized by one standard deviation of the mean

### 3.2 Surface Composition Mapping

#### 3.2.1 XPS of Unreacted and Reacted Surfaces

As described already, the Ca/Al ratio of the unreacted C<sub>3</sub>A is about 15 % higher than the stoichiometric value of 1.5, both in the bulk (see Section 2) and within ≈2 μm of the sintered surface as measured by EDXS (Table 4). In contrast, the Ca/Al ratio within a few nm of the surface probed by XPS (Table 5) is only 1.21, about 20 % lower than the stoichiometric value, a result also reported by Ball *et al.* [51]. A lower apparent Ca/Al ratio near the surface may be measured because of surface hydroxylation or because the surface terminates with oxygen [51]. Similar behavior has also been reported for other cement minerals [18,52,53].

The XPS data obtained from a C<sub>3</sub>A surface before and after exposure to the flowing water-ethanol solution without sulfate are shown in Table 5. The Ca/Al ratio decreases substantially after dissolution, in agreement with the EDXS data, which suggests that dissolution is either 1) incongruent with Ca<sup>2+</sup> ions preferentially leaching into solution, or 2) congruent but immediately followed by the reprecipitation of a Ca-depleted, Al-rich layer. For the incongruent dissolution possibility, it is assumed that leaching of Ca<sup>2+</sup> is accompanied by diffusion of some other cation, usually protons, to compensate for the resultant charge imbalance and that the hydrogen ions protonate the oxygens that are left uncoordinated by the absence of calcium. The mechanism for the second possibility, coupled interfacial dissolution-reprecipitation (CIDR), has already been described for silicate mineral and glass dissolution [54–58]. Brown [59] compiled metastable phase stability data measured by D'Ans and Eick [60] to show that, if C<sub>3</sub>A dissolves congruently, then the solution should first become supersaturated with respect to a metastable Al(OH)<sub>3</sub> phase before becoming supersaturated with respect to C<sub>4</sub>AH<sub>19</sub> or C<sub>2</sub>AH<sub>8</sub>. This suggests that metastable Al(OH)<sub>3</sub> should form first during congruent C<sub>3</sub>A dissolution, as indicated by the initial amorphous products observed by Breval [61] and Meredith *et al.* [62], before becoming destabilized by growth of C<sub>4</sub>AH<sub>19</sub> [63]. The current data were obtained in flowing solutions that theoretically kept the saturation state low near the surface, so macroscopic crystals of C<sub>4</sub>AH<sub>19</sub> should not precipitate and were not observed by SEM. However, the thin boundary layer adjacent to the surface flows more slowly and can build up some concentration of dissolved ions [64] that might still favor the formation of metastable Al(OH)<sub>3</sub> or other aluminum-rich phase. These thermodynamic tendencies, together with the current data and evidence from previous

studies [8–11], strongly imply that an Al-rich surface layer develops during early C<sub>3</sub>A dissolution. Further study, such as with transmission electron microscopy, is necessary to further investigate the CIDR mechanism [54–58].

Table 5. XPS Results for a C<sub>3</sub>A Surface Exposed to a Water-Ethanol Solution

Sample	Surface Condition	No. of Locations Examined	Ca/Al Ratio	
			Average	Standard Deviation
Unreacted	Original	5	1.03	0.053
	Sputtered (Ar <sup>+</sup> )	3	1.21	0.036
60% ethanol, 30 min, 33 mL min <sup>-1</sup> flow rate	Original	5	0.72	0.027
	Sputtered (Ar <sup>+</sup> )	3	0.85	0.074

### 3.2.2 TOF-SIMS of C<sub>3</sub>A Surfaces with Sulfate Solutions

The continuous surface sputtering provided by TOF-SIMS was used to obtain depth profiles of the surface composition. Sputtering depth was estimated from the sputtering time by measuring the sputter rate and modeling it as a piecewise linear function, as described in the Appendix. The initial sputter rate from 0 s to 500 s differed from the rate between 500 s and 6000 s. The TOF-SIMS scanned a 120 nm diameter cesium ion beam over a 100 μm × 100 μm area, producing a large footprint that causes artificial broadening of the profiles in Figure 6, since an average depth is estimated over a large area with presumed non-uniform depths of these elemental distributions. It must also likely that sputtering depths are somewhat non-uniform at a given location, since there is some surface roughness and the sample does contain some porosity, which can further lead to artificial broadening in the profiles. Therefore, the ratio profiles in Figure 6 and the elemental profiles in Figure A.4 are sigmoidal in shape. Despite these complications, significant trends in the relative concentrations of Ca and Al as a function of depth can be compared and contrasted.

The Ca/Al intensity ratio profiles from TOF-SIMS, which should not be confused with actual molar ratios,<sup>§</sup> are shown in Figure 6a,b as a function of sputtering time and depth, respectively. The data were collected from at least two locations on each sample (see Figure A.3). As discussed in the Appendix, some of the samples had very similar Ca/Al intensity ratios at each surface location, in which cases Figure 6 shows the average profile. For the sample dissolved in water, two of the three measured locations had similar profiles, so the average of those two is plotted along with the data from the third location. The sample dissolved in MgSO<sub>4</sub> solution exhibited slightly different trends at the two locations, so both are included in Figure 6. In all cases, Figure 6 shows that the Ca/Al ratio is a minimum at the surface and sharply increases toward a uniform bulk value between 3.7 and 4.1.

Figure 7 shows the intensity ratio of the solution cation (Mg, K, or Na) to Ca as a function of depth, indicating a cation-specific preference for penetrating the solid. Specifically, Mg penetrates to the greatest extent, K only slightly, and Na not at all. This explains why the EDXS data in Table 4 show a prominent signal for Mg but not for the alkali cations. The K/Ca

<sup>§</sup> Due to intrinsically different elemental sputter rates, the actual (true) molar ratios could not be obtained from the data. However, comparisons of the relative intensity ratios still reflect the trends in the composition profiles.

profile in Figure 7 varies somewhat among the sampling locations, so the EDXS data may have been collected from a location with low K/Ca content, such as Location 2 in Figure 7. Cubic  $C_3A$  can accommodate approximately 1 % equivalent alkali ( $Na_2O + 0.66 K_2O$ ) [1], but Figure 7 suggests that, while these alkalis can be present in clinker  $C_3A$ , they do not appear to significantly penetrate or adsorb on the surface during  $C_3A$  dissolution.

Figure 8 compares the Mg/Ca and Ca/Al intensity ratio profiles for the sample exposed to  $MgSO_4$  solution. These profiles imply that  $Mg^{2+}$  substitutes for  $Ca^{2+}$  in the near-surface crystal structure because the higher Mg/Ca tracks with lower Ca/Al. As should be expected, the Mg/Ca intensity ratio approaches zero with increasing depth below the surface as the Ca/Al intensity ratio increases toward its bulk value of approximately 4.

Some heterogeneity in the interactions of the solution components with surface is observed from one location to another. For the three water-exposed surfaces, two sampling areas behaved similarly to the control (shown as Water Average in Figure 6) while another area behaved more like the sulfate-exposed samples (shown as Water Location 1 in Figure 6). This agrees with the previous findings from Brand and Bullard [12], who demonstrated that dissolution rates on polycrystalline  $C_3A$  surfaces vary widely from one location to another. Furthermore,  $C_3A$  can undergo a large-scale dissolution event which appears to sweep away a uniformly thick surface layer from the entire field of view after about 30 min of exposure to flowing water-ethanol solutions identical to those used in this study (see Figure 9 in Ref. [12]). The cause of the event was unknown at the time, but, in light of the current data, may have been a Ca-depleted layer (like that in Figure 6) reaching a critical thickness and losing mechanical integrity. Perhaps the two water samples shown in Figure 6 with behavior similar to the control (*i.e.*, labeled Water Average) are such locations where the top layer has been dissolved, revealing sections of similar composition to the control.

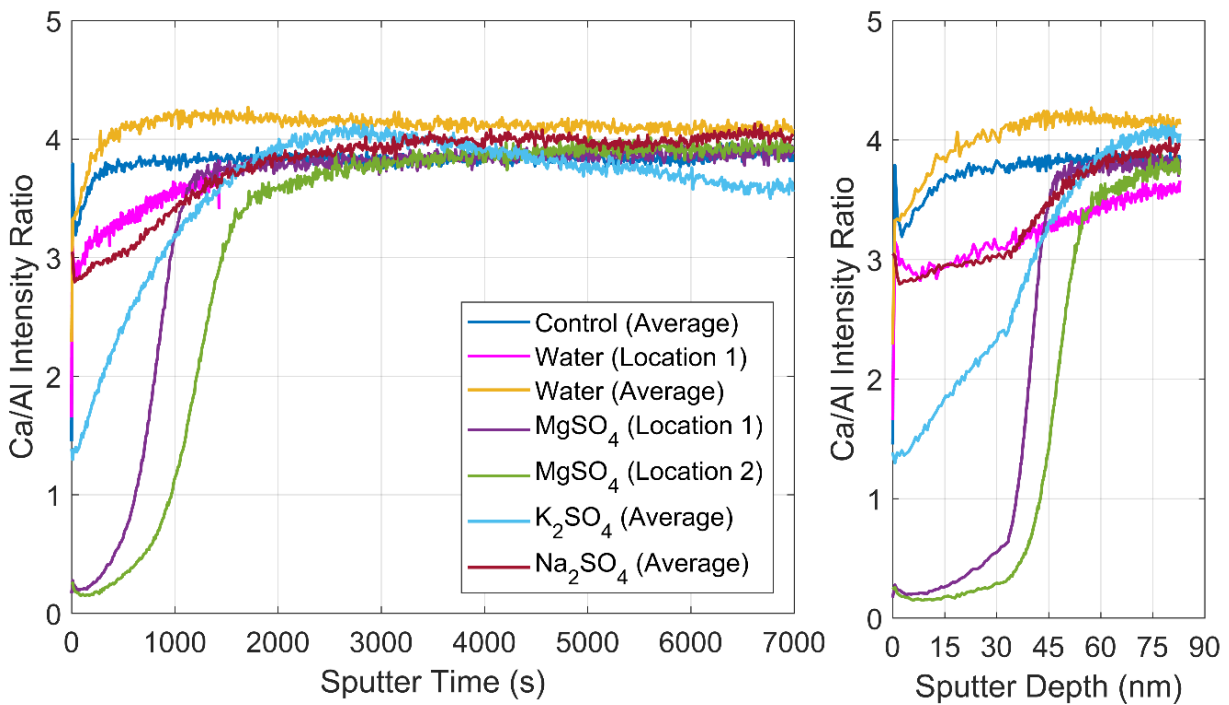


Figure 6. Ca/Al intensity ratios determined from TOF-SIMS: plotted with sputter time (left) and estimated mean sputter depth until 3000 s sputter time (right). Data collected at a single location are labeled as such. Curves labeled as “Average” are the average profile from two locations exhibiting very similar composition profiles (see Appendix).

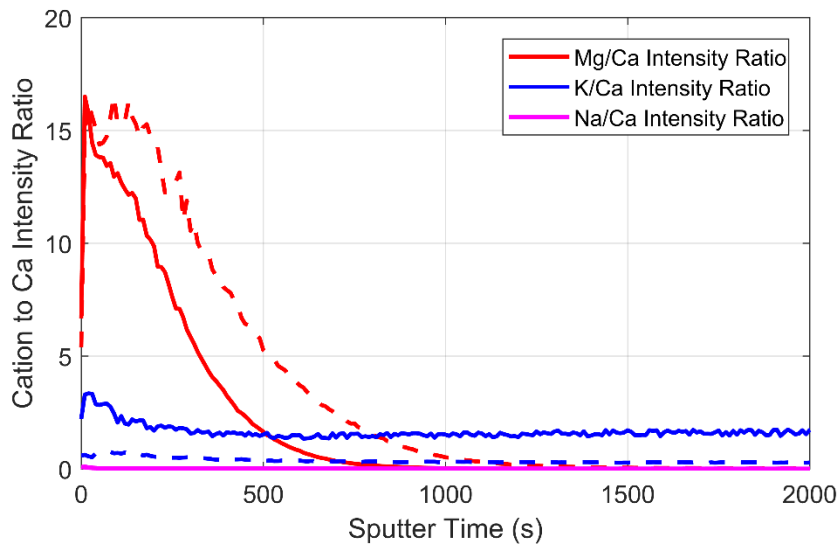


Figure 7. Cation to Ca intensity ratios for Location 1 (solid line) and Location 2 (dashed line) on the samples exposed to sulfate solutions. The sputtering time extended to 7000 s but the profiles are relatively constant after 2000 s.

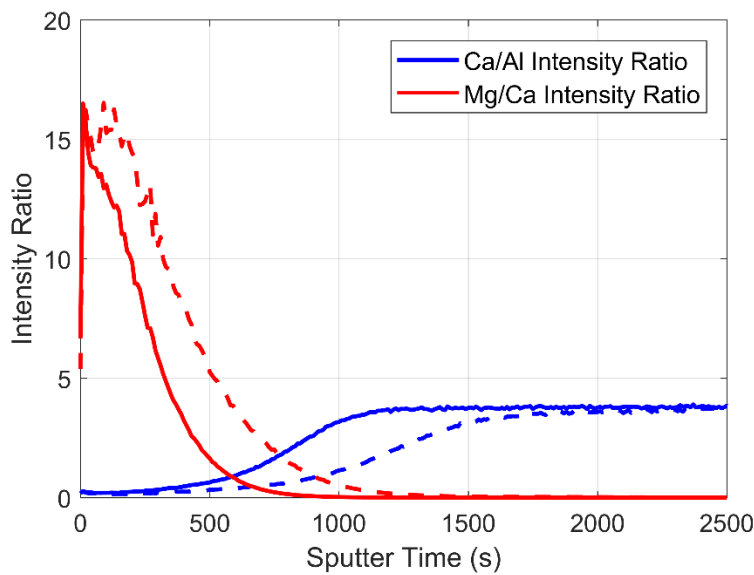


Figure 8. Intensity ratios for Location 1 (solid line) and Location 2 (dashed line) for the sample exposed to  $\text{MgSO}_4$  solution. The sputtering time extended to 7000 s but the profiles are relatively constant after 2500 s.

While negative sulfur ions, such as would be present in adsorbed sulfate ions at the surface, could not be tracked by the TOF-SIMS, two cesium-sulfur ion complexes,  $\text{Cs}_2\text{S}^+$  and  $\text{CsS}^+$ , could be detected and were used as proxies for sulfur to provide approximate sulfur depth profiles (Figure 9). The  $\text{Cs}_2\text{S}^+$  signal is stronger than that of  $\text{CsS}^+$  for the  $\text{MgSO}_4$  and  $\text{Na}_2\text{SO}_4$  samples, but the  $\text{CsS}^+$  signal is stronger for the  $\text{K}_2\text{SO}_4$  samples (see Figure A.9). The intensity ratio depth profiles of  $(\text{Cs}_2\text{S}+\text{CsS})/\text{Al}$  in Figure 9 show a strong sulfur presence in the samples exposed to  $\text{MgSO}_4$ , a moderate sulfur presence from  $\text{Na}_2\text{SO}_4$ , and almost no sulfur from  $\text{K}_2\text{SO}_4$ . The  $\text{Cs}_2\text{S}/\text{Al}$  intensity ratio appears to reach a constant for an estimated few tens of nanometers before diminishing to a relatively constant value.

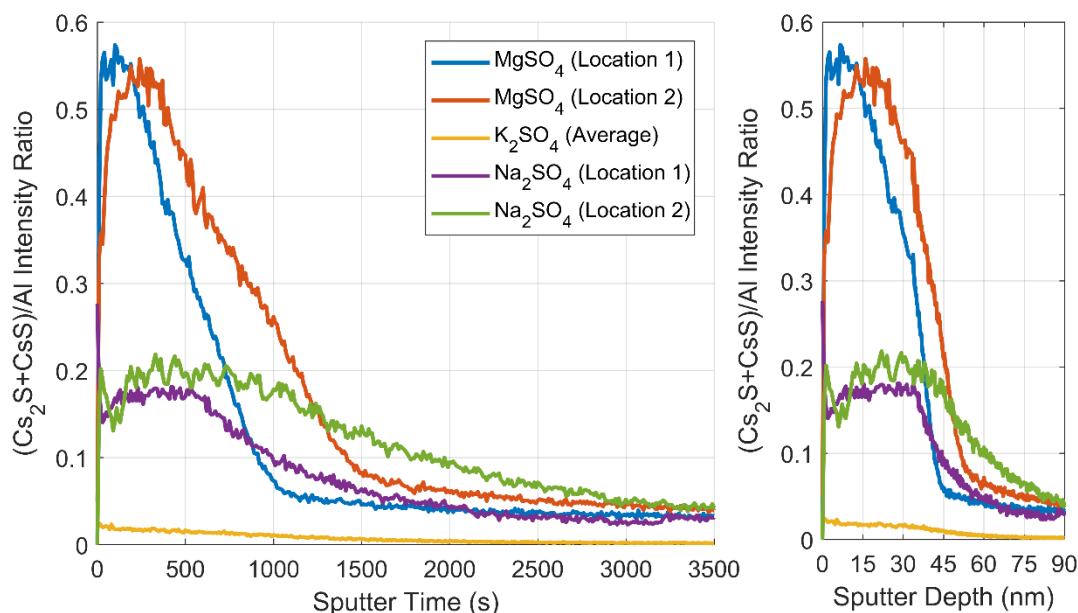


Figure 9.  $(\text{Cs}_2\text{S}+\text{CsS})/\text{Al}$  intensity ratios at each of the two locations for the samples exposed to  $\text{MgSO}_4$ ,  $\text{K}_2\text{SO}_4$ , and  $\text{Na}_2\text{SO}_4$ . The sputtering time extended to 7000 s but the profiles are relatively constant after 3500 s. The estimated mean sputter depth is also shown. Ratios from both  $\text{K}_2\text{SO}_4$  samples are shown as the average since the trends were approximately equivalent.

### 3.3 Initial Hydration of $\text{C}_3\text{A}$

Motivated by the cationic and sulfate ion effects on the  $\text{C}_3\text{A}$  dissolution rate and surface composition, *in situ* SRXRD experiments were performed to further evaluate their influences on the  $\text{C}_3\text{A}$  hydration process and especially on the characteristics and timing of crystalline hydration product precipitation. At least two replicate XRD experiments were performed using each sulfate salt solution, although the experiments in water and in  $10 \text{ mmol L}^{-1} \text{K}_2\text{SO}_4$  only yielded one usable dataset. Figure 10 shows the time-dependent XRD data, which indicate very rapid changes in phase proportions. For  $\text{C}_3\text{A}$  in water (Figure 10a), these data are similar to the results of other synchrotron studies (*e.g.*, [35]) in that precipitation occurs within seconds. Hydration in each of the sulfate solutions produces qualitatively similar evolution of the various diffraction peaks with time (Figure 10b–h).

Figure 11 shows time segments from Figure 10c for hydration in calcium sulfate solution. The primary peak at  $2.67 \text{ \AA}$  corresponds to cubic  $\text{C}_3\text{A}$  [35], which diminishes over time as that phase dissolves. The broad peak centered at  $10.65 \text{ \AA}$  is the primary peak for hydroxy-AFm ( $\text{C}_4\text{AH}_{19}$ ), which has been observed to occur at  $10.7 \text{ \AA}$  [35,39,65–67] or at  $10.64 \text{ \AA}$  (PDF 42-487). Hydrogarnet ( $\text{C}_3\text{AH}_6$ ) has a primary peak at  $2.29 \text{ \AA}$  (PDF 24-217), but the weaker peak at  $4.44 \text{ \AA}$  is often used as a more resolvable characteristic peak [35,41]; both peaks are evident in Figure 11. Ettringite has primary peaks at  $9.72 \text{ \AA}$  and  $5.61 \text{ \AA}$  [49], but neither of these are observed in Figure 11 (also see Figure A.11). This suggests that the only calcium sulfoaluminate phase to form in these experiments may be a sulfate-AFm, the stoichiometrically-pure form of which is called monosulfoaluminate. The primary peak for monosulfoaluminate should be located at approximately  $8.93 \text{ \AA}$  (PDF 1-83-1289), but none of the peaks in Figure 11 are found

at that exact location. By 2 h of hydration, a broad peak appears at 8.3 Å and another broad shoulder peak forms between 8.5 Å and 10 Å. Figure 12a shows a peak at 10.65 Å forming between 0 min and 45 min, which was already identified as C<sub>4</sub>AH<sub>19</sub>, and also shows the shoulder peak between 8.5 Å and 10 Å. Figure 12b indicates that this shoulder peak and the larger peak at 10.65 Å diminish between 45 min and 120 min while a broad peak at 8.3 Å becomes stronger. The reduced d-spacing of this peak compared to the 8.93 Å for pure sulfate-AFm, together with the broad shoulder peak from 8.5 Å to 10 Å, might indicate a solid solution of hydroxy- and carbonate-AFm phases, as reported by Matschei *et al.* [68]. For comparison, hemicarboaluminate and monocarboaluminate phases should have peaks at approximately 8.2 Å and 7.6 Å, respectively [68]. The peak position can also be influenced by the hydration state, that is the number of water molecules per formula unit, of the sulfate-AFm phase [67,69]. However, the lower hydration states are unlikely to have formed here because they are stable only at low relative humidities [67,69,70] and the pore volumes in these experiments were saturated with solution. In addition, this same shoulder peak also appears when C<sub>3</sub>A is hydrated in the absence of sulfate ions (see Figure A.12), which rules out the peak's identification as a sulfate-AFm phase. And because a low sulfate solution concentration was utilized here compared to the sulfate concentration in typical portland cement pore solutions, the broad shoulder peak between 8.5 Å and 10 Å can probably be attributed to a solid solution of AFm phases. The solid solution probably has a predominantly hemicarboaluminate structure at later ages because that phase is associated with the more distinct but broad peak at 8.3 Å and because the diminishing peak at 10.65 Å is assigned specifically to C<sub>4</sub>AH<sub>19</sub>.

Minard *et al.* [2] proposed that phase evolution during the first 30 s of C<sub>3</sub>A hydration is the same whether or not dissolved sulfates are available: C<sub>3</sub>A dissolution is followed by precipitation of a hydroxy-AFm phase. Figure 10 provides some support for that because it shows both C<sub>4</sub>AH<sub>19</sub> and the AFm solid solution precipitating with and without available sulfates. However, those phases appear considerably later than 30 s in sulfate solutions (Figure 10b-h) compared to deionized water (Figure 10a, Figure A.12). We are not currently able to explain this difference in time of initial precipitation in sulfate solutions compared to Minard's study. The latter used saturated gypsum (16 mmol L<sup>-1</sup>) solutions or saturated gypsum-portlandite solutions (27 mmol L<sup>-1</sup> Ca, 13 mmol L<sup>-1</sup> S, and 25 mmol L<sup>-1</sup> OH<sup>-</sup>) [2] instead of 10 mmol L<sup>-1</sup> gypsum used here, but a higher sulfate concentration in solution would not seem to promote faster hydroxy-AFm precipitation.

Quantitative Rietveld analysis of these data was not attempted because reliable structure models for some hydroxy-AFm phases, including C<sub>4</sub>AH<sub>19</sub> and C<sub>4</sub>AH<sub>13</sub>, are not available and because the AFm components may be solid solutions. Even so, information about the timing and order of phase formation can be obtained from the time dependence of the major peak intensities. The primary peaks used for that purpose are 2.67 Å for cubic C<sub>3</sub>A, 4.44 Å for C<sub>3</sub>AH<sub>6</sub>, 10.65 Å for C<sub>4</sub>AH<sub>19</sub>, and ≈0.83 Å for the AFm solid solution, respectively. The intensities were all scaled by the initial peak intensity for cubic C<sub>3</sub>A. Figure 13 shows examples from the CaSO<sub>4</sub> and MgSO<sub>4</sub> experiments (see Figure A.13 for all plots). The C<sub>3</sub>A intensity decreases with time as it dissolves, following the characteristic sigmoidal curve that is usually observed for aluminates and silicates during hydration (*e.g.*, [35,37,71–75]). C<sub>4</sub>AH<sub>19</sub> forms after about 10 min to 20 min and reaches a maximum between 40 min and 80 min, depending on the solution. The AFm solid

solution attains a maximum at approximately the same time as  $C_4AH_{19}$ . The solid solution remains stable thereafter, but the  $C_4AH_{19}$  evidently becomes unstable relative to  $C_3AH_6$  [1], which reaches a maximum and remains constant as the  $C_4AH_{19}$  content decreases.

$C_3AH_6$  and the AFm solid solution appear to precipitate shortly after  $C_4AH_{19}$  in the sulfate solutions. Table 6 shows the estimated times at which  $C_4AH_{19}$  is first detected and also the time of its peak intensity. As already mentioned, initial precipitation is delayed in the sulfate solution compared to pure water, although no cation-specific effects are observed. Christensen *et al.* [39] found that hydroxy-AFm and sulfate-AFm formed within 5 min of water being added to a mixture of  $C_3A$  and gypsum powders. Table 6 shows that these phases did not form as quickly as Christensen *et al.* observed, likely because the sulfate ions are already in solution to retard  $C_3A$  dissolution in this study, whereas sulfate concentrations started at zero and were limited by the rate of gypsum dissolution in Christensen's experiments.

The XRD patterns for  $C_3A$  in pure deionized water (Figure 10a) include a few strong and persistent peaks at 2.06 Å and 1.79 Å. These lattice spacings are characteristic of a face centered cubic metal such as iron, nickel, or chromium, and likely originate from the stainless steel sample holder. These peaks do not contribute to the subsequent analysis because the initial peak intensity of  $C_3A$  is used as the reference. Closer examination of Figure 10a (also see Figure A.12 and Figure A.13a) reveals that the hydrated phases are present at the start of the experiment; water evidently contacted the powder just before data collection started, because the  $C_4AH_{19}$  peak intensity at 10.7 Å is not strong at the beginning and increases steadily with time; previous studies have shown that the peak at 10.7 Å can occur as soon as 10 s to 20 s after introduction of water to  $C_3A$  [35].

To evaluate any cation-specific effects on the precipitated phases, the time dependence of peak positions were examined for  $C_3AH_6$  at 4.44 Å,  $C_4AH_{19}$  at 10.65 Å, and AFm solid solution at  $\approx 8.3$  Å. For the deionized water experiment, the  $C_3AH_6$  and  $C_4AH_{19}$  peak positions remain relatively constant at 4.44 Å and 10.67 Å, respectively (Figure 14); no AFm solid solution peak position is included for the deionized water experiment because, unlike its behavior in the sulfate solutions (Figure 12b), the shoulder peak never diminished to reveal a stronger peak (Figure A.12). In sulfate solutions, the peak positions of all the major hydration products are more variable in time than in water. This implies that the unit cell parameters of both  $C_4AH_{19}$  and the AFm solid solution change slightly with time, which could be caused by gradual changes in hydration states or interlayer ion composition. The  $C_3AH_6$  peak position changes only a little and approaches 4.43 Å after 2 h in nearly all experiments. This implies that the  $C_3AH_6$  structure, unlike those of the other detected AFm phases, is not influenced by the type of cation in solution.

The AFm phases have a hexagonal unit cell [1] with unit cell parameters,  $a$  and  $c$ , that are related to the d-spacing of a given (hkl) plane,  $d_{hkl}$ , according to [76]

$$\frac{1}{d_{hkl}^2} = \frac{4}{3} \left( \frac{h^2 + hk + k^2}{a^2} \right) + \frac{l^2}{c^2} \cdot \quad (4)$$

The  $C_4AH_{19}$  peak at 10.65 Å corresponds to the (006) plane with  $a$  and  $c$  being 5.74 Å and 63.85 Å, respectively (PDF 42-487). The AFm solid solution peak at 8.3 Å most closely correlates with the main peak for hemicarboaluminate (006) plane at 8.1 Å, for which  $a = 5.78$  Å and  $c = 48.81$  Å [48]. Because the  $a$  parameter of all these AFm phases is approximately 5.7 Å to 5.9 Å [1], the XRD patterns can be analyzed with Eq. (4) to estimate the time dependence of the  $c$  parameter,

as shown in Figure 14. The  $c$  parameter depends on the interlayer water content and the interlayer anion [1], so Figure 14 can provide additional insights about how solution composition can dynamically affect the AFm crystal structures as they grow. Table 7 shows that the  $c$  parameter of the AFm solid solution is greater than that of hemicarboaluminate (48.81 Å [48]) and that its basal spacing,  $d_{006}$ , is less than that of monosulfoaluminate (8.93 Å). Together, these observations suggest that the AFm solid solution is likely incorporating various anions, like  $\text{OH}^-$ ,  $\text{SO}_4^{2-}$ , and  $\text{CO}_3^{2-}$ , in the interlayer. Table 7 also shows that the basal spacing (and therefore the  $c$  parameter) of  $\text{C}_4\text{AH}_{19}$  produced in sulfate solutions is slightly lower than in deionized water, and therefore suggests some involvement of cations or sulfate ions in solution. However, the inferred  $\text{C}_4\text{AH}_{19}$   $c$  parameter in sulfate solutions is still within 1 % of published value of 63.85 Å (PDF 42-487).

Figure 15 shows time snapshots of the XRD patterns in Figure 10. The steady increase in the background with time suggests that an amorphous phase grows concurrently with the crystalline phases. The background due to the glass capillary has already been subtracted from the patterns, so any additional increase in the background with time can be attributed to an amorphous phase. Breval [61] concluded from microscopic observations that an amorphous gel, probably  $\text{Al}(\text{OH})_3$  [59], is the initial hydration product to form on  $\text{C}_3\text{A}$  at temperatures  $< 60^\circ\text{C}$ . Meredith *et al.* [62] also reported an amorphous gel within the first few minutes of  $\text{C}_3\text{A}$  hydration prior to the precipitation of crystalline phases whether or not calcium sulfate was present.

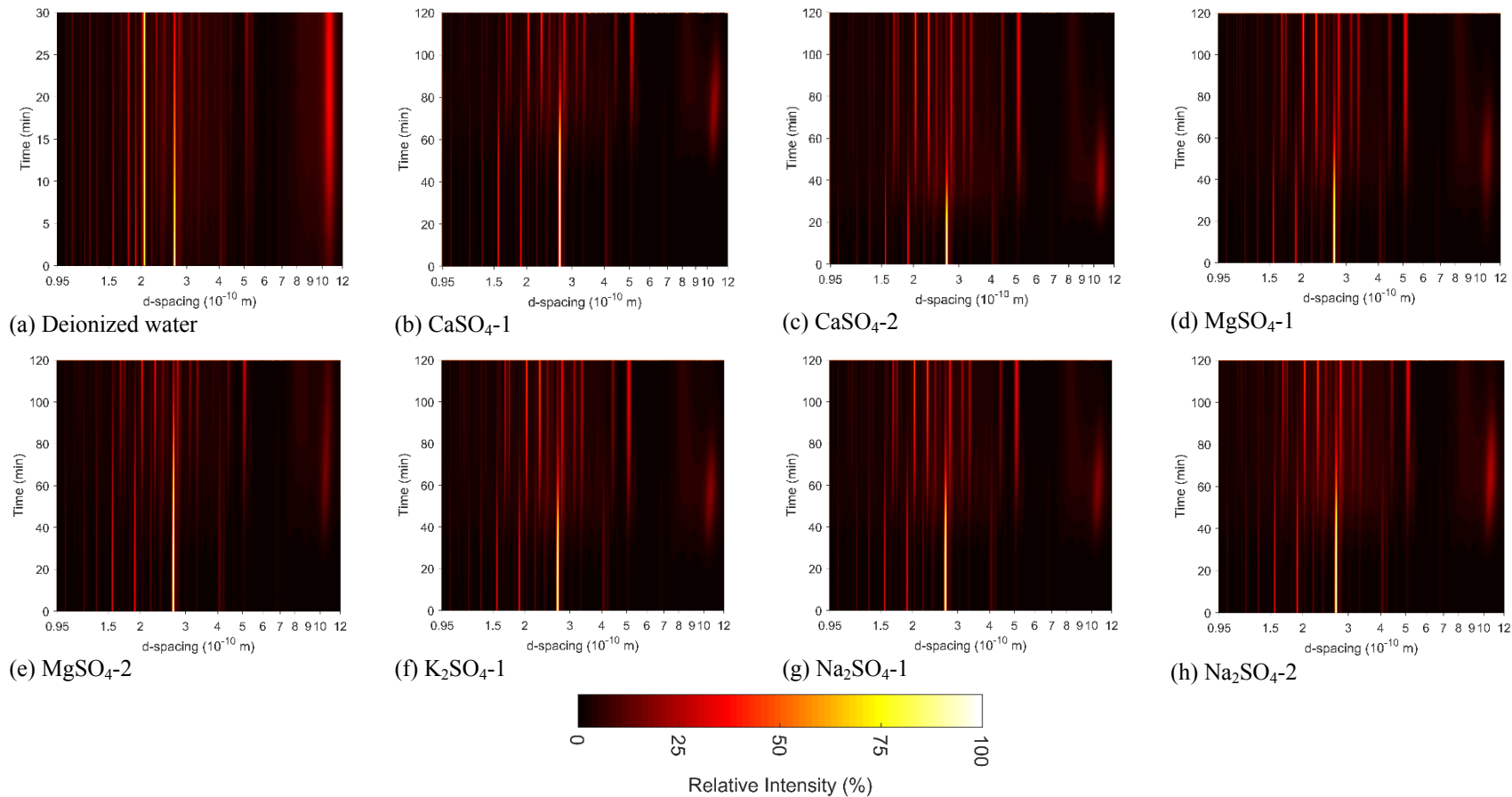


Figure 10. Background-subtracted synchrotron XRD results for  $\text{C}_3\text{A}$  hydration as a function of time (vertical axis) in (a) deionized water and  $10 \text{ mmol L}^{-1}$  solutions of (b,c)  $\text{CaSO}_4$ , (d,e)  $\text{MgSO}_4$ , (f)  $\text{K}_2\text{SO}_4$ , and (g,h)  $\text{Na}_2\text{SO}_4$ . The color bar shown represents the intensity relative to that of the initial  $\text{C}_3\text{A}$  primary peak intensity at  $2.67 \text{ \AA}$ .

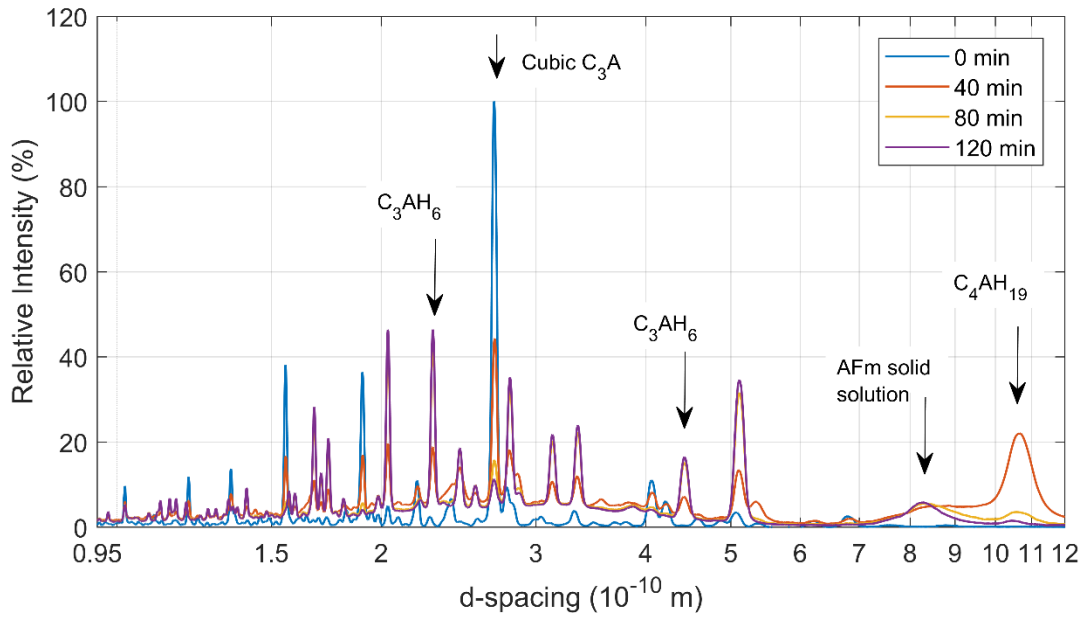
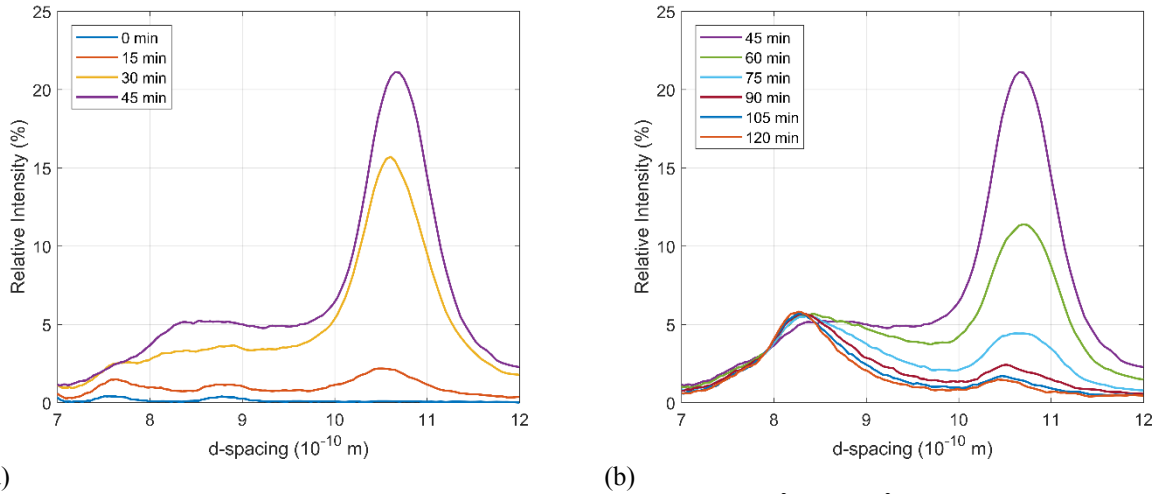
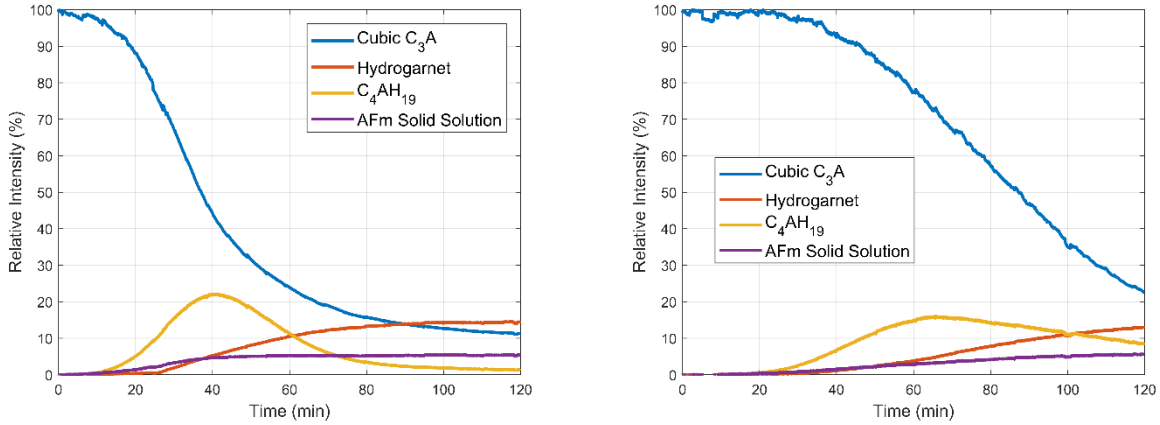


Figure 11. Time segments Figure 10c, highlighting the characteristic peaks as discussed in the text.



(a) (b)  
 Figure 12. Time segments from Figure 10c windowed from 7 Å to 12 Å for (a) 0 min to 45 min and (b) 45 min to 120 min.



(a) (b)  
 Figure 13. Relative XRD peak intensities for each phase during hydration in solutions of (a)  $\text{CaSO}_4$  (Figure 10c) and (b)  $\text{MgSO}_4$  (Figure 10e). See Figure A.13 for all plots.

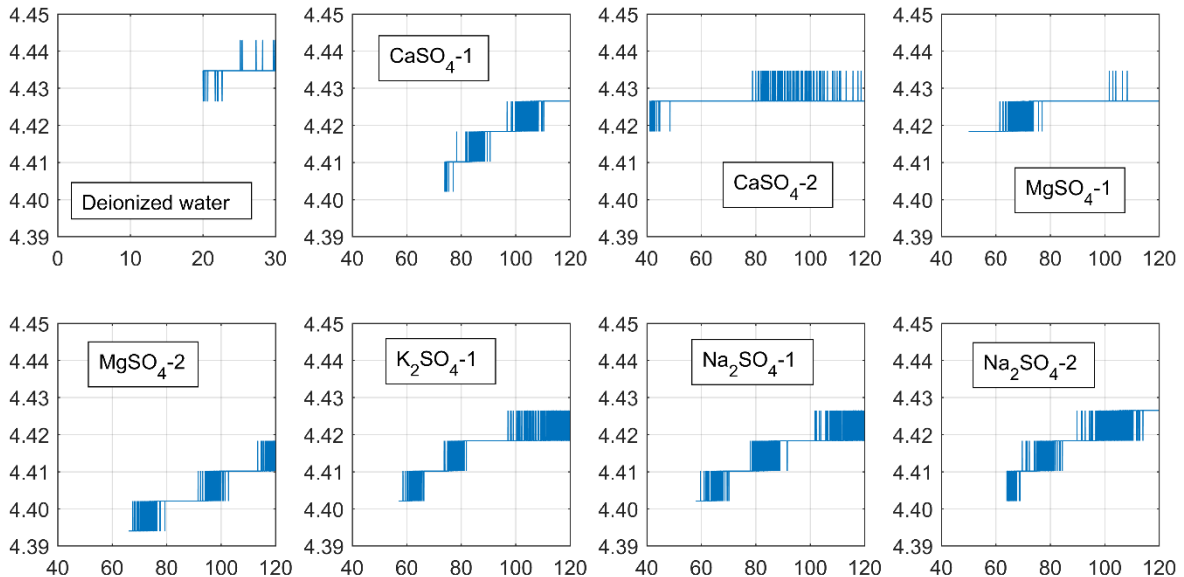
Table 6. Time of Initial Precipitation

Experiment*	Time of Initial Precipitation (min)**	Maximum Relative Intensity of $\text{C}_4\text{AH}_{19}$ (%)	Time of Maximum Relative Intensity of $\text{C}_4\text{AH}_{19}$ (min)
Deionized water	0***	37	24
$\text{CaSO}_4$ -1	37	21	74
$\text{CaSO}_4$ -2	10	22	41
$\text{MgSO}_4$ -1	5	16	50
$\text{MgSO}_4$ -2	20	17	66
$\text{K}_2\text{SO}_4$ -1	15	19	57
$\text{Na}_2\text{SO}_4$ -1	21	18	58
$\text{Na}_2\text{SO}_4$ -2	21	25	64

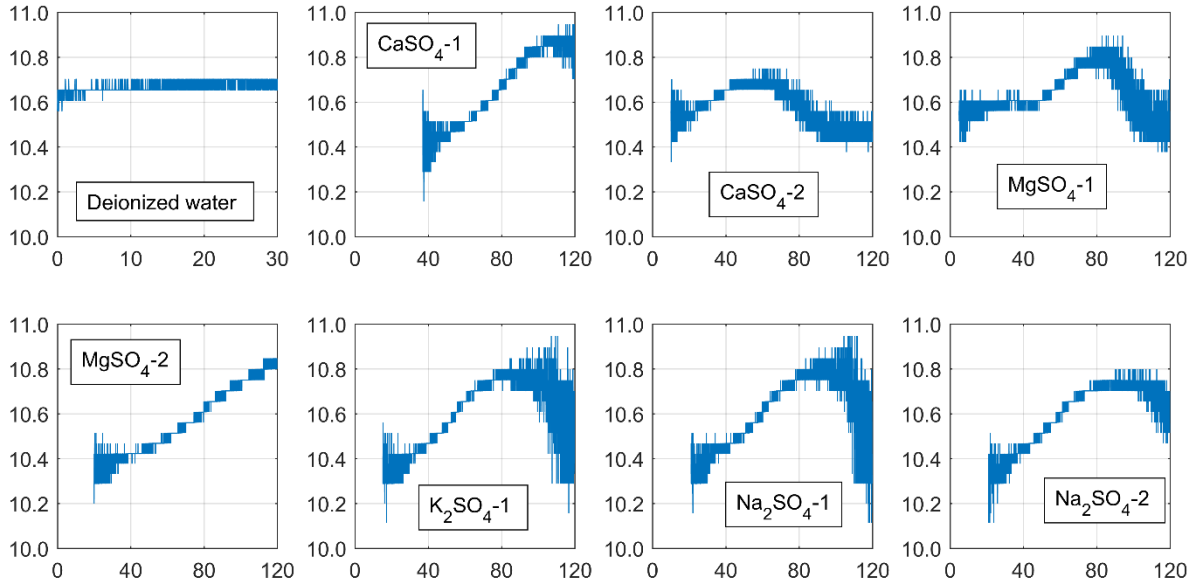
\*Following the notion in Figure 10

\*\*Estimated as the time when  $\text{C}_4\text{AH}_{19}$  reaches 0.5% relative intensity

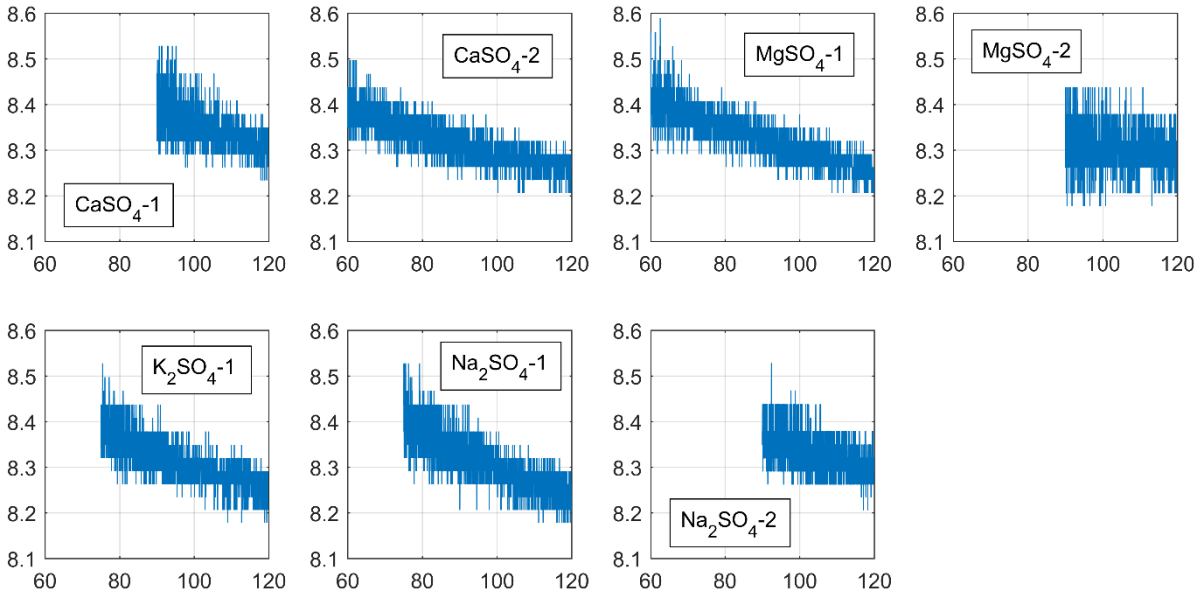
\*\*\*Precipitated phases detected at the start of data collection



(a)  $C_3AH_6$



(b)  $C_4AH_{19}$



(c) AFm solid solution

Figure 14. Changes in peak positions with hydration time: (a)  $C_3AH_6$ , (b)  $C_4AH_{19}$ , and (c) AFm solid solution. The ordinate is in units of  $10^{-10}$  m ( $\text{\AA}$ ) and the abscissa is in units of min.  $C_3AH_6$  is presented starting from the time of maximum  $C_4AH_{19}$  intensity, and  $C_4AH_{19}$  is presented starting from the time of initial precipitation. The AFm solid solution phase is presented starting from the approximate time at which the shoulder peak diminished and a stronger peak was evident.

Table 7. AFm Phase Basal Spacing and Estimated Unit Cell Parameter  $c$

Experiment Identification	$C_4AH_{19}$ Basal Spacing (nm) from Figure 14b		Unit Cell Parameter $c$ for $C_4AH_{19}$ (nm)	AFm Solid Solution Basal Spacing (nm) from Figure 14c		Unit Cell Parameter $c$ for AFm Solid Solution (nm)
	Range	Mean (Standard Deviation)		Range	Mean (Standard Deviation)	
Water	1.056 to 1.070	1.067 (0.003)	$6.402 \pm 0.018$	N/A	N/A	N/A
CaSO <sub>4</sub> -1	1.016 to 1.095	1.066 (0.016)	$6.396 \pm 0.096$	0.823 to 0.853	0.834 (0.004)	$5.004 \pm 0.024$
CaSO <sub>4</sub> -2	1.033 to 1.075	1.058 (0.010)	$6.348 \pm 0.060$	0.821 to 0.850	0.832 (0.005)	$4.992 \pm 0.030$
MgSO <sub>4</sub> -1	1.038 to 1.090	1.063 (0.010)	$6.378 \pm 0.060$	0.821 to 0.859	0.833 (0.005)	$4.998 \pm 0.030$
MgSO <sub>4</sub> -2	1.020 to 1.085	1.057 (0.015)	$6.342 \pm 0.090$	0.818 to 0.844	0.830 (0.005)	$4.980 \pm 0.030$
K <sub>2</sub> SO <sub>4</sub> -1	1.011 to 1.095	1.060 (0.016)	$6.360 \pm 0.096$	0.818 to 0.853	0.831 (0.005)	$4.986 \pm 0.030$
Na <sub>2</sub> SO <sub>4</sub> -1	1.011 to 1.095	1.061 (0.016)	$6.366 \pm 0.096$	0.818 to 0.853	0.831 (0.006)	$4.986 \pm 0.036$
Na <sub>2</sub> SO <sub>4</sub> -2	1.011 to 1.080	1.060 (0.014)	$6.360 \pm 0.084$	0.821 to 0.853	0.833 (0.005)	$4.998 \pm 0.030$

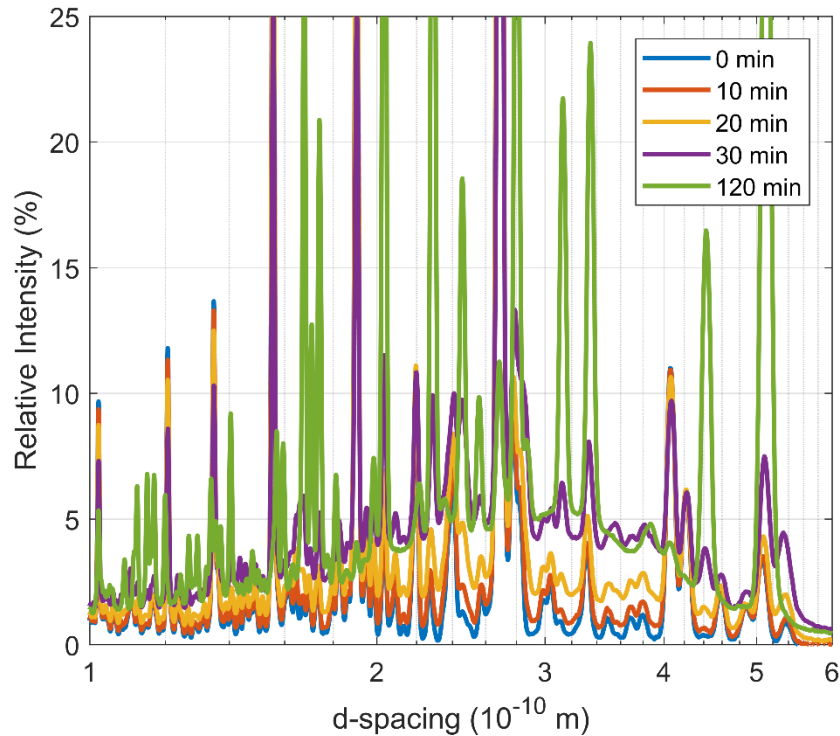


Figure 15. Time segments from Figure 10c windowed from 1 Å to 6 Å to highlight the increase in background during the first 30 min, which suggests that an amorphous phase grows along with the crystalline phases after about 10 min (Table 6).

#### 4. DISCUSSION

The data strongly indicate that sulfate solutions influence both the *precipitation* of hydration products and the *dissolution* of  $C_3A$ . For instance, solutions of 10 mmol L<sup>-1</sup> MgSO<sub>4</sub> reduce the median  $C_3A$  dissolution rate by about 40 % compared to water (Table 1), although the large IQR calls into question the significance of this reduction. In contrast, the same MgSO<sub>4</sub> solution delays the onset of precipitation from 0 min in water to anywhere between 5 min and 20 min, and the attainment of maximum  $C_4AH_{19}$  content takes about twice as long (Table 6). Similar delays in precipitation also happen in the other sulfate solutions examined here (CaSO<sub>4</sub>, Na<sub>2</sub>SO<sub>4</sub>, and K<sub>2</sub>SO<sub>4</sub>).

#### 4.1 Sulfate Effects on Dissolution

Previous studies have concluded that sulfate adsorption to  $C_3A$  is somehow responsible for regulating its hydration rate [2–8]. However, this study demonstrated that  $C_3A$  dissolution rates plateau with increasing  $MgSO_4$  concentrations (Table 1). This suggests that there are a finite number of defect sites that sulfate is adsorbing to, thereby retarding dissolution, so further increases in sulfate concentration do not additionally diminish the dissolution rate past a certain concentration. Since dissolution continues to proceed in the presence of sulfate ions, even though the rate is decreased relative to no sulfate in solution, this suggests that sulfate ions are only affecting certain dissolution-reactive surface sites. However, it should be noted that sulfate is also adsorbing to surface sites that are not actively dissolving, at least not on a scale measurable by the DHM.

Figure 9 indicates that sulfur is present within the top few tens of nanometers of the surface, which supports the previous literature about adsorption of sulfate ions or ion complex adsorption to  $C_3A$  [2–8], but it is uncertain why there is such a great difference between the three cations. One hypothesis concerns the presence of ethanol in the solution: knowing that the electrostatic attraction between an anion and cation in solution is inversely proportional to the medium's dielectric constant [77], this attractive force is about 65 % stronger at 20 °C in the water-ethanol mixture than it is in pure water.\*\* Therefore, one might expect a relatively greater concentration of sulfate ion complexes in the water-ethanol solution than would be predicted by equilibrium speciation calculations in pure water, which would correspond to a relatively lower concentration of  $SO_4^{2-}$  ions in water-ethanol solutions and could decrease the concentration of adsorbed  $SO_4^{2-}$ . However, this argument should be true for all three sulfate salts, so it does not explain the trends in Figure 9. Furthermore, the electric field at the surface of  $K^+$  is less than that of  $Na^+$ ,  $Ca^{2+}$ , or  $Mg^{2+}$ ,†† which means that the strength of the ion pair in solution should be weakest for  $K^+$ .

Another hypothesis regarding the trends in Figure 9 is that there are cation-specific effects on the electric double layer. The Debye length, an estimate of the thickness of the diffuse layer, is inversely proportional to the square root of ionic strength [78]. The estimated Debye length, assuming that the ionic strength of the double layer is equivalent to that in the bulk solution, is similar for all three solutions: 4.4 nm for  $Na_2SO_4$  and  $K_2SO_4$  and 3.8 nm for  $MgSO_4$ . However, the ionic concentrations in the double layer should be expected to not be equivalent to the bulk solution. At circumneutral pH,  $C_3A$  has a negative surface charge [8,9], so cations in solution will adsorb to the surface in the Stern layer. Geometrically, the relatively larger  $K^+$  ions will not pack as efficiently at the Stern layer as the smaller  $Na^+$  or  $Mg^{2+}$  ions, so the effectiveness of screening the negative  $C_3A$  surface charge based on the cation size can be anticipated to follow the trend  $Mg^{2+} > Na^+ > K^+$ , which agrees with the relative trends in Figure 9. Indeed the

---

\*\* The dielectric constant at 20 °C for the water-ethanol mixture is estimated to be 48 [100]. The dielectric constant of pure water is approximately 80 at 20 °C [100].

†† Considering a cation as a charged sphere, the electric field at the surface is related to  $z/r^2$  [77], where  $z$  is the charge number and  $r$  is the ionic radius. The effective ionic radius of  $Ca^{2+}$ ,  $Mg^{2+}$ ,  $K^+$ , and  $Na^+$  is 0.100 nm, 0.072 nm, 0.138 nm, and 0.102 nm [50], respectively, so  $z/r^2$  is 200 nm<sup>-2</sup>, 386 nm<sup>-2</sup>, 53 nm<sup>-2</sup>, and 96 nm<sup>-2</sup> for  $Ca^{2+}$ ,  $Mg^{2+}$ ,  $K^+$ , and  $Na^+$ , respectively.

zeta potential of C<sub>3</sub>A in 13 mmol L<sup>-1</sup> K<sub>2</sub>SO<sub>4</sub> solution appears to be slightly less than the zeta potential in 13 mmol L<sup>-1</sup> CaSO<sub>4</sub> solution [8].

The final argument for the trends in Figure 9 is with regard to ettringite precipitation, which would naturally increase the sulfur concentration measured at the surface. Ettringite precipitation was not observed on the surface of samples exposed to less than 10 mmol L<sup>-1</sup> (Figure 5), which was confirmed by SEM after the dissolution experiments by DHM. Therefore, no precipitation is anticipated to have occurred on the TOF-SIMS samples exposed to only 1 mmol L<sup>-1</sup>. However, the TOF-SIMS samples were not explicitly examined by SEM like the DHM samples were.

#### **4.2 Cationic Effects on Dissolution**

Dissolution of C<sub>3</sub>A is accompanied by a significant decrease in its near-surface Ca/Al ratio (Section 3.2). Whether that is caused by incongruent dissolution [8,9,11], by the formation of a thin Ca-depleted, Al-rich surface layer, or a combination of both, the surface is relatively enriched in hydroxylated aluminates and depleted of Ca (Section 3.2.1). TOF-SIMS reveals that this lower Ca/Al ratio at the surface increases continuously with depth toward a constant bulk value. Contact with MgSO<sub>4</sub> solutions yields both the lowest Ca/Al ratios at the surface and the most gradual recovery of Ca/Al with depth. Within this context, the data will be discussed with regard to cation exchange and CIDR mechanisms.

##### **4.2.1 Cation Exchange Mechanism**

Specific ion effects, as embodied in the Hofmeister (lyotropic) series, are likely involved in such interactions during dissolution of minerals [79–82] and cementitious solids (*e.g.*, C<sub>3</sub>S [83–85]). One assumption is that the dissolution follows an interdiffusion, cation exchange mechanism. The relative affinity for selective surface ion exchange, which generally increases with ion charge density and decreases with hydrated ionic radius, follows the ordering Ca<sup>2+</sup> > Mg<sup>2+</sup> > K<sup>+</sup> > Na<sup>+</sup> [86]. Indeed, the TOF-SIMS data reveal a relatively high surface concentration of Mg, a small presence of K, and no Na near the reacted C<sub>3</sub>A surface, which tracks well with the Hofmeister series ordering. However, there must be some other driving force causing the Ca<sup>2+</sup> to first dissociate from the C<sub>3</sub>A solid as well as a secondary mechanism driving force for a different cation to substitute at Ca<sup>2+</sup> vacancies in the solid according to the relative affinities Mg<sup>2+</sup> > K<sup>+</sup> > Na<sup>+</sup>. Indeed this cation exchange process is initiated by an H<sup>+</sup> ion from solution, which will displace of a cation in the solid [87]; that cation is Ca<sup>2+</sup> from the C<sub>3</sub>A in this case. At this stage we merely speculate that the flow-through conditions used in these experiments maintain a relatively high local concentration of the solution cations Mg<sup>2+</sup>, K<sup>+</sup>, or Na<sup>+</sup> compared to the Ca<sup>2+</sup> cations which are generated by dissolution but then flushed away to maintain nearly constant undersaturation relative to C<sub>3</sub>A.‡‡ With the release of Ca<sup>2+</sup> ions, protonation of aluminate tetrahedra and breaking of the alumina ring structure [12,88] occurs to release Al(OH)<sub>4</sub><sup>-</sup> into solution. During this process, it is possible that Mg<sup>2+</sup> in the electric double layer could migrate to some of the Ca<sup>2+</sup> vacancies to compensate the charge imbalance there. Since Mg<sup>2+</sup> is about 30 %

---

‡‡ Based on the highest mean dissolution flux in the presence of sulfate (Table 2) and the solution flow rate, the estimated Ca<sup>2+</sup> concentration in the outflow solution is on the order of 10<sup>-6.7</sup> mol L<sup>-1</sup>, which is significantly less than the inflow sulfate concentration of 10<sup>-3</sup> mol L<sup>-1</sup>.

smaller than  $\text{Ca}^{2+}$ , it can more easily fit at those sites than  $\text{K}^+$  or  $\text{Na}^+$ , both of which offer a charge imbalance and are further removed in the Hofmeister series. Again, this explanation is speculative but has the merit of tracking with the cation/Al ratios in Figure 7 and of accounting for the observation that  $\text{Mg}^{2+}$  has a significant retarding influence on  $\text{C}_3\text{A}$  dissolution (Table 2). If this explanation is correct, then the apparent cation exchange behavior observed in Section 3.2 may be an artefact of the flowing solution conditions. In static solutions where dissolved  $\text{Ca}^{2+}$  ions are not kept low near the surface,  $\text{Ca}^{2+}$  ions or  $\text{CaSO}_4^0$  ion complexes in the double layer could potentially adsorb to the surface, which would agree with the proposition by Mishra *et al.* [88] that amorphous  $\text{Ca}(\text{OH})_2$  precipitates at the aluminate surface.

However, if an interdiffusion mechanism is assumed, then this would suggest that the diffusion rates are rather high, particularly for  $\text{Mg}^{2+}$ , which was present in appreciable concentrations up to an estimated depth of at least 30 nm (Figure 6) over the 30 min dissolution experiment.

Further study is needed to assess this behavior.

#### 4.2.2 CIDR Mechanism

An alternative assumption is that  $\text{C}_3\text{A}$  dissolution follows a CIDR mechanism. Hellmann *et al.* [55] present characteristics and processes indicative of CIDR: 1) stoichiometric dissolution of the solid mineral within a thin fluid boundary layer, regardless of solution pH; 2) a porous, amorphous layer reprecipitates at the interface; and 3) the amorphous layer forms regardless of bulk solution saturation conditions, even in undersaturated conditions. Therefore, by this mechanism, it would be assumed that  $\text{C}_3\text{A}$  dissolves congruently (such as at etch pits), releasing ions into a thin boundary layer of solution. Despite the flowing solution conditions, there is still a no flow boundary layer at the interface [64], resulting in a supersaturated boundary layer [89] and the reprecipitation of a Ca-depleted, Al-rich surface layer that is expected to be amorphous. The nonstoichiometric Ca/Al ratio in solution, such as shown by Myers *et al.* [11], suggests an *apparent* incongruent dissolution as a result of the CIDR mechanism.

Thus, the reduction in the Ca/Al ratio at the surface (Table 5 and Figure 6) and very low dissolved Al content in the solution [11] are supporting evidence of a CIDR mechanism. The evidence of an amorphous phase (Figure 15) can either be evidence of a CIDR mechanism or of a macroscopic amorphous phase precipitation (as discussed in Section 3.3).

Furthermore, the apparent massive dissolution event observed for  $\text{C}_3\text{A}$  previously (see Figure 9 in Ref. [12]) could also be evidence of a CIDR mechanism, wherein the reprecipitated surface layer is not adhered to the surface and it is subsequently removed during the dissolution process; this may also explain the different behaviors of the water samples in Figure 6, as discussed previously. Studies have suggested that the CIDR-resultant surface layer is not strongly adhered to the surface [90,91].

The Al intensity was found to not vary significantly as a function depth, whereas Ca and cation intensities were found to vary dramatically with depth in some instances (Figure A.4). This behavior is additionally supportive of a CIDR mechanism, as similar behavior has been observed in other CIDR studies [55,57].

The CIDR mechanism can also explain the cation-to-Ca ratio behavior in Figure 7, wherein the reprecipitated layer forms with the inclusion of  $\text{Mg}^{2+}$  or  $\text{K}^+$ , which replaces the

discussion in Section 4.2.1. The literature provides evidence of this behavior, such as a reprecipitated K-enriched layer on Na-feldspar exposed to KCl solution [92]. It is still unclear, however, why there is a rank of relative affinity  $Mg^{2+} > K^+ > Na^+$ . One potential response is with regard to the relative hydroxide solubilities, which are  $Mg(OH)_2 \ll KOH \approx NaOH$ . This would indicate that reprecipitated surface layer is enriched in Mg relative to the other cations because  $Mg(OH)_2$  has such a low solubility.

Based on the evidence presented herein, it is not possible to definitively conclude which mechanism(s) is governing dissolution. Further study, such as with transmission electron microscopy [54–58], is required to further assess the CIDR mechanism.

#### **4.3 Effects on Precipitation**

Compared to water, sulfate salt solutions significantly alter the overall early hydration kinetics of  $C_3A$ , as shown by the SRXRD measurements in Section 3.3. The rate of  $C_3A$  dissolution is decreased in these solutions, the first appearance of solid hydration products is delayed, and the subsequent growth of those products is slower.

The non-bridging oxygens of aluminate groups at the  $C_3A$  surface are hydroxylated [51,88] even before contact with liquid water. Surface hydroxylation has also been measured on anhydrous  $C_3S$  [93], which were hydroxylated  $Q^0$  silica groups, and on portland cement grains [94,95]. Our TOF-SIMS measurements in Section 3.2 imply that calcium is depleted from the surface in contact with solution. At the same time, sulfate anions or ion complexes can adsorb to that hydrous alumina layer by displacing hydroxyl groups [96], which is reminiscent of the concept of ion pair adsorption offered by Myers *et al.* [8]. The retarding influence on the dissolution of aluminate ions can thereby delay nucleation and slow the growth of solid hydration products such as  $C_3AH_6$  and phases in the AFm family. Not surprisingly, the retarding effect of sulfate has been reported for other hydrous minerals. For example, the dissolution of ferrihydrite is diminished by sulfate [97,98] as two hydroxyl groups at the surface are replaced by one sulfate anion [99]. The adsorbed sulfate, in turn, has been shown to retard, for example, the formation of goethite from schwertmannite [97].

## **5. CONCLUSIONS**

The effects of low concentrations of sulfate salts on the dissolution and early hydration of cubic  $C_3A$  was investigated by *in situ* dissolution experiments, by *ex situ* surface analysis, and *in situ* synchrotron X-ray diffraction. The results indicate that even low sulfate concentrations (1 mmol  $L^{-1}$ ) of  $MgSO_4$ ,  $K_2SO_4$ , and  $Na_2SO_4$  can reduce the median dissolution rate of  $C_3A$ , although the reduction is around 40 %, with the effect of  $Na_2SO_4$  being less significant than  $MgSO_4$  or  $K_2SO_4$ . Under flowing solution conditions, a plateau in the median dissolution rate is observed with increasing  $MgSO_4$  concentration, which suggests that sulfate ions may only affect a finite number of active dissolution sites.

Relatively high surface concentrations of Mg are observed after some dissolution. Much less K and almost no Na are observed at the surface after dissolution, so that adsorption affinity of the solution cation conforms to the lyotropic series. This suggests that, as the Ca cations leave the  $C_3A$  surface during dissolution, some of the available sites may get occupied by other cations in solution, such as through an interdiffusion mechanism. However, an alternative interpretation

of this behavior was posited as occurring through a coupled interfacial dissolution-precipitation mechanism. Regardless, further study is needed to assess which mechanism is governing.

Rather low concentrations ( $10 \text{ mmol L}^{-1}$ ) of  $\text{CaSO}_4$ ,  $\text{MgSO}_4$ ,  $\text{K}_2\text{SO}_4$ , and  $\text{Na}_2\text{SO}_4$  retard the precipitation of hydrous phases, namely  $\text{C}_3\text{AH}_6$  and other AFm-type phases. Knowing that the  $\text{C}_3\text{A}$  surface is enriched in Al during dissolution, it seems likely that the retarding influence of sulfate ions on  $\text{C}_3\text{A}$  hydration has the same basic mechanism as for ferrihydrite dissolution: sulfate ions adsorb to the hydrous alumina in the  $\text{C}_3\text{A}$  surface, retard the release of Al-bearing species into solution, and thereby delay the precipitation of the hydrous calcium aluminate phases.

## ACKNOWLEDGMENTS

The *in situ* X-ray diffraction is based upon research conducted at the Cornell High Energy Synchrotron Source (CHESS) which is supported by the National Science Foundation under award DMR-1332208. The surface chemical mapping was conducted at the Center for Nanophase Materials Sciences, which is a Department of Energy Office of Science User Facility. For the research conducted in Sections 3.1 and 3.3, ASB acknowledges the National Research Council (NRC) for funding through an NRC Postdoctoral Research Associateship at the National Institute of Standards and Technology (NIST). LaKisha Perry and Max Peltz (NIST) performed the inductively coupled plasma optical emission spectroscopy and particle size distribution analyses, respectively. The authors thank Roland Hellmann (Institute for Earth Sciences, Université Grenoble Alpes) and J. Donald Rimstidt (Virginia Tech) for useful discussions.

## REFERENCES

- [1] H.F.W. Taylor, *Cement Chemistry*, 2nd ed., Thomas Telford, London, 1997.
- [2] H. Minard, S. Garrault, L. Regnaud, A. Nonat, Mechanisms and parameters controlling the tricalcium aluminate reactivity in the presence of gypsum, *Cem. Concr. Res.* 37 (2007) 1418–1426. doi:10.1016/j.cemconres.2007.06.001.
- [3] J.W. Bullard, H.M. Jennings, R.A. Livingston, A. Nonat, G.W. Scherer, J.S. Schweitzer, K.L. Scrivener, J.J. Thomas, Mechanisms of cement hydration, *Cem. Concr. Res.* 41 (2011) 1208–1223. doi:10.1016/j.cemconres.2010.09.011.
- [4] K.L. Scrivener, P. Juilland, P.J.M. Monteiro, Advances in understanding hydration of Portland cement, *Cem. Concr. Res.* 78 (2015) 38–56. doi:10.1016/j.cemconres.2015.05.025.
- [5] R.F. Feldman, V.S. Ramachandran, The influence of  $\text{CaSO}_4 \cdot 2\text{H}_2\text{O}$  upon the hydration character of  $3\text{CaO} \cdot \text{Al}_2\text{O}_3$ , *Mag. Concr. Res.* 18 (1966) 185–196. doi:10.1680/mac.1966.18.57.185.
- [6] K.L. Scrivener, A. Nonat, Hydration of cementitious materials, present and future, *Cem. Concr. Res.* 41 (2011) 651–665. doi:10.1016/j.cemconres.2011.03.026.
- [7] G. Artioli, J.W. Bullard, Cement hydration: The role of adsorption and crystal growth, *Cryst. Res. Technol.* 48 (2013) 903–918. doi:10.1002/crat.201200713.
- [8] R.J. Myers, G. Geng, J. Li, E.D. Rodríguez, J. Ha, P. Kidkhunthod, G. Sposito, L.N. Lammers, A.P. Kirchheim, P.J.M. Monteiro, Role of adsorption phenomena in cubic tricalcium aluminate dissolution, *Langmuir.* 33 (2017) 45–55. doi:10.1021/acs.langmuir.6b03474.
- [9] M.E. Tadros, W.Y. Jackson, J. Skalny, Study of the dissolution and electrokinetic

- behavior of tricalcium aluminate, in: M. Kerker (Ed.), *Colloid Interface Sci. Vol. IV*, Academic Press, New York, 1976: pp. 211–223.
- [10] J. Skalny, M.E. Tadros, Retardation of tricalcium aluminate hydration by sulfates, *J. Am. Ceram. Soc.* 60 (1977) 174–175. doi:10.1111/j.1151-2916.1977.tb15503.x.
- [11] R.J. Myers, G. Geng, E.D. Rodriguez, P. da Rosa, A.P. Kirchheim, P.J.M. Monteiro, Solution chemistry of cubic and orthorhombic tricalcium aluminate hydration, *Cem. Concr. Res.* 100 (2017) 176–185. doi:10.1016/j.cemconres.2017.06.008.
- [12] A.S. Brand, J.W. Bullard, Dissolution kinetics of cubic tricalcium aluminate measured by digital holographic microscopy, *Langmuir.* 33 (2017) 9645–9656. doi:10.1021/acs.langmuir.7b02400.
- [13] C. Fischer, R.S. Arvidson, A. Lüttge, How predictable are dissolution rates of crystalline material?, *Geochim. Cosmochim. Acta.* 98 (2012) 177–185. doi:10.1016/j.gca.2012.09.011.
- [14] C. Fischer, I. Kurganskaya, T. Schäfer, A. Lüttge, Variability of crystal surface reactivity: What do we know?, *Appl. Geochemistry.* 43 (2014) 132–157. doi:10.1016/j.apgeochem.2014.02.002.
- [15] C. Fischer, I. Kurganskaya, A. Luttge, Inherited control of crystal surface reactivity, *Appl. Geochemistry.* 91 (2018) 140–148. doi:10.1016/j.apgeochem.2018.02.003.
- [16] C. Fischer, A. Luttge, Pulsating dissolution of crystalline matter, *Proc. Natl. Acad. Sci.* 115 (2018) 897–902. doi:10.1073/pnas.1711254115.
- [17] A. Luttge, R.S. Arvidson, C. Fischer, I. Kurganskaya, Kinetic concepts for quantitative prediction of fluid-solid interactions, *Chem. Geol.* 504 (2019) 216–235. doi:10.1016/j.chemgeo.2018.11.016.
- [18] A.S. Brand, J.M. Gorham, J.W. Bullard, Dissolution rate spectra of  $\beta$ -dicalcium silicate in water of varying activity, *Cem. Concr. Res.* in press (2019).
- [19] Y. Levenson, S. Emmanuel, Pore-scale heterogeneous reaction rates on a dissolving limestone surface, *Geochim. Cosmochim. Acta.* 119 (2013) 188–197. doi:10.1016/j.gca.2013.05.024.
- [20] S. Emmanuel, Mechanisms influencing micron and nanometer-scale reaction rate patterns during dolostone dissolution, *Chem. Geol.* 363 (2014) 262–269. doi:10.1016/j.chemgeo.2013.11.002.
- [21] P. Juilland, E. Gallucci, Morpho-topological investigation of the mechanisms and kinetic regimes of alite dissolution, *Cem. Concr. Res.* 76 (2015) 180–191. doi:10.1016/j.cemconres.2015.06.001.
- [22] C. Fischer, A. Luttge, Beyond the conventional understanding of water-rock reactivity, *Earth Planet. Sci. Lett.* 457 (2017) 100–105. doi:10.1016/j.epsl.2016.10.019.
- [23] M. Michaelis, C. Fischer, L.C. Ciacchi, A. Luttge, Variability of zinc oxide dissolution rates, *Environ. Sci. Technol.* 51 (2017) 4297–4305. doi:10.1021/acs.est.6b05732.
- [24] A.S. Brand, P. Feng, J.W. Bullard, Calcite dissolution rate spectra measured by in situ digital holographic microscopy, *Geochim. Cosmochim. Acta.* 213 (2017) 317–329. doi:10.1016/j.gca.2017.07.001.
- [25] P. Feng, A.S. Brand, L. Chen, J.W. Bullard, In situ nanoscale observations of gypsum dissolution by digital holographic microscopy, *Chem. Geol.* 460 (2017) 25–36. doi:10.1016/j.chemgeo.2017.04.008.
- [26] I. Bibi, R.S. Arvidson, C. Fischer, A. Lüttge, Temporal evolution of calcite surface dissolution kinetics, *Minerals.* 8 (2018) 256. doi:10.3390/min8060256.

- [27] S. Joseph, J. Skibsted, Ö. Cizer, A quantitative study of the C<sub>3</sub>A hydration, *Cem. Concr. Res.* 115 (2019) 145–159. doi:10.1016/j.cemconres.2018.10.017.
- [28] B.A. Clark, P.W. Brown, Formation of ettringite from tricalcium aluminate and magnesium sulphate, *Adv. Cem. Res.* 12 (2000) 137–142.
- [29] M. Collepardi, G. Baldini, M. Pauri, M. Corradi, Tricalcium aluminate hydration in the presence of lime, gypsum or sodium sulfate, *Cem. Concr. Res.* 8 (1978) 571–580. doi:10.1016/0008-8846(78)90040-6.
- [30] M. Collepardi, G. Baldini, M. Pauri, M. Corradi, Retardation of tricalcium aluminate hydration by calcium sulfate, *J. Am. Ceram. Soc.* 62 (1979) 33–35. doi:10.1111/j.1151-2916.1979.tb18800.x.
- [31] A.S. Brand, Phase uncertainty in digital holographic microscopy measurements in the presence of solution flow conditions, *J. Res. Natl. Inst. Stand. Technol.* 122 (2017) 022 1-41. doi:10.6028/jres.122.022.
- [32] A. Lüttge, R.S. Arvidson, Reactions at surfaces: A new approach integrating interferometry and kinetic simulations, *J. Am. Ceram. Soc.* 93 (2010) 3519–3530. doi:10.1111/j.1551-2916.2010.04141.x.
- [33] A. Lüttge, E.W. Bolton, A.C. Lasaga, An interferometric study of the dissolution kinetics of anorthite: the role of reactive surface area, *Am. J. Sci.* 299 (1999) 652–678. doi:10.2475/ajs.299.7-9.652.
- [34] D.P. Bentz, P. V. Coveney, E.J. Garboczi, M.F. Kleyn, P.E. Stutzman, Cellular automaton simulations of cement hydration and microstructure development, *Model. Simul. Mater. Sci. Eng.* 2 (1994) 783–808.
- [35] A.C. Jupe, X. Turrillas, P. Barnes, S.L. Colston, C. Hall, D. Häusermann, M. Hanfland, Fast in situ x-ray-diffraction studies of chemical reactions: A synchrotron view of the hydration of tricalcium aluminate, *Phys. Rev. B.* 53 (1996) R14697–R14700. doi:10.1103/PhysRevB.53.R14697.
- [36] P. Barnes, X. Turrillas, A.C. Jupe, S.L. Colston, D. O’Connor, R.J. Cernik, P. Livesey, C. Hall, D. Bates, R. Dennis, Applied crystallography solutions to problems in industrial solid-state chemistry: Case examples with ceramics, cements and zeolites, *J. Chem. Soc. Faraday Trans.* 92 (1996) 2187–2196. doi:10.1039/FT9969202187.
- [37] P. Barnes, S. Colston, B. Craster, C. Hall, A. Jupe, S. Jacques, J. Cockcroft, S. Morgan, M. Johnson, D. O’Connor, M. Bellotto, Time- and space-resolved dynamic studies on ceramic and cementitious materials, *J. Synchrotron Radiat.* 7 (2000) 167–77. doi:10.1107/S0909049500003137.
- [38] M.A.G. Aranda, Recent studies of cements and concretes by synchrotron radiation crystallographic and cognate methods, *Crystallogr. Rev.* 22 (2016) 150–196. doi:10.1080/0889311X.2015.1070260.
- [39] A.N. Christensen, T.R. Jensen, J.C. Hanson, Formation of ettringite, Ca<sub>6</sub>Al<sub>2</sub>(SO<sub>4</sub>)<sub>3</sub>(OH)<sub>12</sub>·26H<sub>2</sub>O, AFt, and monosulfate, Ca<sub>4</sub>Al<sub>2</sub>O<sub>6</sub>(SO<sub>4</sub>)·14H<sub>2</sub>O, AFm-14, in hydrothermal hydration of Por, *J. Solid State Chem.* 177 (2004) 1944–1951. doi:10.1016/j.jssc.2003.12.030.
- [40] M. Merlini, G. Artioli, T. Cerulli, F. Cella, A. Bravo, Tricalcium aluminate hydration in additivated systems. A crystallographic study by SR-XRPD, *Cem. Concr. Res.* 38 (2008) 477–486. doi:10.1016/j.cemconres.2007.11.011.
- [41] G. Geng, R.J. Myers, Y.-S. Yu, D.A. Shapiro, R. Winarski, P.E. Levitz, D.A.L. Kilcoyne, P.J.M. Monteiro, Synchrotron X-ray nanotomographic and spectromicroscopic study of

- the tricalcium aluminate hydration in the presence of gypsum, *Cem. Concr. Res.* 111 (2018) 130–137. doi:10.1016/j.cemconres.2018.06.002.
- [42] D.E. Boyce, J.V. Bernier, *heXRD: Modular, Open Source Software for the Analysis of High Energy X-ray Diffraction Data*, Lawrence Livermore National Laboratory, 2013. doi:10.2172/1062217.
- [43] B.H. Toby, R.B. Von Dreele, GSAS-II: The genesis of a modern open-source all purpose crystallography software package, *J. Appl. Crystallogr.* 46 (2013) 544–549. doi:10.1107/S0021889813003531.
- [44] W. Wong-Ng, H. McMurdie, B. Paretzkin, C. Hubbard, A. Dragoo, PDF 38-1429, ICDD Grant-in-Aid, 1987.
- [45] R. Allmann, Refinement of the hybrid layer structure  $[\text{Ca}_2\text{Al}(\text{OH})_6]^+[\frac{1}{2}(\text{SO}_4)\cdot 3\text{H}_2\text{O}]^-$ , *Neues Jahrb. Für Mineral. Monatshefte.* (1977) 136–144.
- [46] H. Kuzel, H. Pöllmann, PDF 42-487, ICDD Grant-in-Aid, 1991.
- [47] H.E. Swanson, H.F. McMurdie, M.C. Morris, E.H. Evans, B. Paretzkin, J.H. de Groot, S.J. Carmel, *Monograph 25: Standard X-ray Diffraction Powder Patterns, Section 11*, National Bureau of Standards, Washington D.C., 1974.
- [48] T. Runčevski, R.E. Dinnebier, O. V. Magdysyuk, H. Pöllmann, Crystal structures of calcium hemicarboaluminate and carbonated calcium hemicarboaluminate from synchrotron powder diffraction data research papers, *Acta Crystallogr. B* 68 (2012) 493–500. doi:10.1107/S010876811203042X.
- [49] J. Goetz-Neunhoffer, F. Neubauer, Refined ettringite  $(\text{Ca}_6\text{Al}_2(\text{SO}_4)_3(\text{OH})_{12}\cdot 26\text{H}_2\text{O})$  structure for quantitative X-ray diffraction analysis, *Powder Diffr.* 21 (2006) 4–11. doi:10.1154/1.2146207.
- [50] R.D. Shannon, Revised effective ionic radii and systematic studies of interatomic distances in halides and chalcogenides, *Acta Crystallogr. A* 32 (1976) 751–767. doi:10.1107/S0567739476001551.
- [51] M.C. Ball, R.E. Simmons, I. Sutherland, Surface composition of anhydrous tricalcium aluminate and calcium aluminoferrite, *J. Mater. Sci.* 22 (1987) 1975–1979. doi:10.1007/BF01132926.
- [52] V. Rheinheimer, I. Casanova, An X-ray photoelectron spectroscopy study of the hydration of C2S thin films, *Cem. Concr. Res.* 60 (2014) 83–90. doi:10.1016/j.cemconres.2014.03.005.
- [53] M.C. Ball, R.E. Simmons, I. Sutherland, Surface composition of anhydrous calcium silicates, *Br. Ceram. Proc.* 35 (1985) 1–9.
- [54] R. Hellmann, J.M. Penisson, R.L. Hervig, J.H. Thomassin, M.F. Abrioux, An EFTEM/HRTEM high-resolution study of the near surface of labradorite feldspar altered at acid pH: Evidence for interfacial dissolution-precipitation, *Phys. Chem. Miner.* 30 (2003) 192–197. doi:10.1007/s00269-003-0308-4.
- [55] R. Hellmann, R. Wirth, D. Daval, J.-P. Barnes, J.-M. Penisson, D. Tisserand, T. Epicier, B. Florin, R.L. Hervig, Unifying natural and laboratory chemical weathering with interfacial dissolution-precipitation: A study based on the nanometer-scale chemistry of fluid-silicate interfaces, *Chem. Geol.* 294–295 (2012) 203–216. doi:10.1016/j.chemgeo.2011.12.002.
- [56] D. Daval, R. Hellmann, G.D. Saldi, R. Wirth, K.G. Knauss, Linking nm-scale measurements of the anisotropy of silicate surface reactivity to macroscopic dissolution rate laws: New insights based on diopside, *Geochim. Cosmochim. Acta.* 107 (2013) 121–

134. doi:10.1016/j.gca.2012.12.045.
- [57] R. Hellmann, S. Cotte, E. Cadel, S. Malladi, L.S. Karlsson, S. Lozano-Perez, M. Cabié, A. Seyeux, Nanometre-scale evidence for interfacial dissolution-reprecipitation control of silicate glass corrosion, *Nat. Mater.* 14 (2015) 307–311. doi:10.1038/nmat4172.
- [58] D. Daval, I. Martinez, J.-M. Guigner, R. Hellmann, J. Corvisier, N. Findling, C. Dominici, B. Goffé, F. Guyot, Mechanism of wollastonite carbonation deduced from micro- to nanometer length scale observations, *Am. Mineral.* 94 (2009) 1707–1726. doi:10.2138/am.2009.3294.
- [59] P.W. Brown, Phase equilibria and cement hydration, in: J. Skalny (Ed.), *Mater. Sci. Concr. I*, American Ceramic Society, Westerville, OH, 1989: pp. 73–93.
- [60] J. D'Ans, H. Eick, Das system CaO-Al<sub>2</sub>O<sub>3</sub>-H<sub>2</sub>O bei 20°C und das erhärten der tonerdezemente (The system CaO-Al<sub>2</sub>O<sub>3</sub>-H<sub>2</sub>O at 20°C and the hardening of the alumina cements), *Zement-Kalk-Gips.* 6 (1953) 197–210.
- [61] E. Breval, C<sub>3</sub>A hydration, *Cem. Concr. Res.* 6 (1976) 129–137. doi:10.1016/0008-8846(76)90057-0.
- [62] P. Meredith, A.M. Donald, N. Meller, C. Hall, Tricalcium aluminate hydration: Microstructural observations by in-situ electron microscopy, *J. Mater. Sci.* 39 (2004) 997–1005. doi:10.1023/B:JMSC.0000012933.74548.36.
- [63] J.M. Gaidis, E.M. Gartner, Hydration mechanisms II, in: J. Skalny, S. Mindess (Eds.), *Mater. Sci. Concr. II*, American Ceramic Society, Westerville, OH, 1991: pp. 9–39.
- [64] M. Peruffo, M.M. Mbogoro, M. Adobes-Vidal, P.R. Unwin, Importance of mass transport and spatially heterogeneous flux processes for in situ atomic force microscopy measurements of crystal growth and dissolution kinetics, *J. Phys. Chem. C.* 120 (2016) 12100–12112. doi:10.1021/acs.jpcc.6b03560.
- [65] A.N. Christensen, N.V.Y. Scarlett, I.C. Madsen, T.R. Jensen, J.C. Hanson, Real time study of cement and clinker phases hydration, *Dalt. Trans.* (2003) 1529–1536. doi:10.1039/b301095n.
- [66] A.N. Christensen, T.R. Jensen, N.V.Y. Scarlett, I.C. Madsen, J.C. Hanson, Hydrolysis of pure and sodium substituted calcium aluminates and cement clinker components investigated by in situ synchrotron X-ray powder diffraction, *J. Am. Ceram. Soc.* 87 (2004) 1488–1493. doi:10.1111/j.1551-2916.2004.01488.x.
- [67] L.G. Baquerizo, T. Matschei, K.L. Scrivener, M. Saeidpour, L. Wadsö, Hydration states of AFm cement phases, *Cem. Concr. Res.* 73 (2015) 143–157. doi:10.1016/j.cemconres.2015.02.011.
- [68] T. Matschei, B. Lothenbach, F.P. Glasser, The AFm phase in Portland cement, *Cem. Concr. Res.* 37 (2007) 118–130. doi:10.1016/j.cemconres.2006.10.010.
- [69] L.G. Baquerizo, T. Matschei, K.L. Scrivener, M. Saeidpour, A. Thorell, L. Wadsö, Methods to determine hydration states of minerals and cement hydrates, *Cem. Concr. Res.* 65 (2014) 85–95. doi:10.1016/j.cemconres.2014.07.009.
- [70] O.M. Jensen, P.F. Hansen, E.E. Lachowski, F.P. Glasser, Clinker mineral hydration at reduced relative humidities, *Cem. Concr. Res.* 29 (1999) 1505–1512. doi:10.1016/S0008-8846(99)00132-5.
- [71] J.W. Bullard, B. Lothenbach, P.E. Stutzman, K.A. Snyder, Coupling thermodynamics and digital image models to simulate hydration and microstructure development of portland cement pastes, *J. Mater. Res.* 26 (2011) 609–622. doi:10.1557/jmr.2010.41.
- [72] B. Lothenbach, F. Winnefeld, Thermodynamic modelling of the hydration of Portland

- cement, *Cem. Concr. Res.* 36 (2006) 209–226. doi:10.1016/j.cemconres.2005.03.001.
- [73] D. Ectors, J. Neubauer, F. Goetz-Neunhoeffler, The hydration of synthetic brownmillerite in presence of low Ca-sulfate content and calcite monitored by quantitative in-situ-XRD and heat flow calorimetry, *Cem. Concr. Res.* 54 (2013) 61–68. doi:10.1016/j.cemconres.2013.08.011.
- [74] R. Snellings, G. Mertens, Ö. Cizer, J. Elsen, Early age hydration and pozzolanic reaction in natural zeolite blended cements: Reaction kinetics and products by in situ synchrotron X-ray powder, *Cem. Concr. Res.* 40 (2010) 1704–1713. doi:10.1016/j.cemconres.2010.08.012.
- [75] R. Snellings, G. Mertens, R. Adriaens, J. Elsen, In situ synchrotron X-ray powder diffraction study of the early age hydration of cements blended with zeolite and quartzite fines and water-reducing agent, *Appl. Clay Sci.* 72 (2013) 124–131. doi:10.1016/j.clay.2012.12.002.
- [76] C. Hammond, *The Basics of Crystallography and Diffraction*, 3rd ed., Oxford University Press, Oxford, 2009.
- [77] R. Chang, J.W. Thorman Jr., *Physical Chemistry for the Chemical Sciences*, University Science Books, 2014.
- [78] J.N. Israelachvili, *Intermolecular and Surface Forces*, 3rd ed., Academic Press, 2011.
- [79] E. Ruiz-Agudo, M. Urosevic, C. V. Putnis, C. Rodríguez-Navarro, C. Cardell, A. Putnis, Ion-specific effects on the kinetics of mineral dissolution, *Chem. Geol.* 281 (2011) 364–371. doi:10.1016/j.chemgeo.2011.01.003.
- [80] E. Ruiz-Agudo, M. Kowacz, C. V. Putnis, A. Putnis, The role of background electrolytes on the kinetics and mechanism of calcite dissolution, *Geochim. Cosmochim. Acta.* 74 (2010) 1256–1267. doi:10.1016/j.gca.2009.11.004.
- [81] M. Kowacz, A. Putnis, The effect of specific background electrolytes on water structure and solute hydration: Consequences for crystal dissolution and growth, *Geochim. Cosmochim. Acta.* 72 (2008) 4476–4487. doi:10.1016/j.gca.2008.07.005.
- [82] P.M. Dove, C.A. Czank, Crystal chemical controls on the dissolution kinetics of the isostructural sulfates: Celestite, anglesite, and barite, *Geochim. Cosmochim. Acta.* 59 (1995) 1907–1915. doi:10.1016/0016-7037(95)00116-6.
- [83] L. Nicoleau, E. Schreiner, A. Nonat, Ion-specific effects influencing the dissolution of tricalcium silicate, *Cem. Concr. Res.* 59 (2014) 118–138. doi:10.1016/j.cemconres.2014.02.006.
- [84] P.W. Brown, C.L. Harner, E.J. Prosen, The effect of inorganic salts on tricalcium silicate hydration, *Cem. Concr. Res.* 16 (1986) 17–22. doi:10.1016/0008-8846(86)90063-3.
- [85] B. Mota, T. Matschei, K. Scrivener, The influence of sodium salts and gypsum on alite hydration, *Cem. Concr. Res.* 75 (2015) 53–65. doi:10.1016/j.cemconres.2015.04.015.
- [86] X. Liu, H. Li, W. Du, R. Tian, R. Li, X. Jiang, Hofmeister effects on cation exchange equilibrium: Quantification of ion exchange selectivity, *J. Phys. Chem. C.* 117 (2013) 6245–6251. doi:10.1021/jp312682u.
- [87] A. Bauer, B.D. Velde, *Geochemistry at the Earth's Surface*, Springer, Berlin, 2014. doi:10.1007/978-3-642-31359-2.
- [88] R.K. Mishra, L. Fernández-Carrasco, R.J. Flatt, H. Heinz, A force field for tricalcium aluminate to characterize surface properties, initial hydration, and organically modified interfaces in atomic resolution, *Dalt. Trans.* 43 (2014) 10602–10616. doi:10.1039/c4dt00438h.

- [89] F. Renard, A. Røyne, C. V. Putnis, Timescales of interface-coupled dissolution-precipitation reactions on carbonates, *Geosci. Front.* 10 (2019) 17–27. doi:10.1016/j.gsf.2018.02.013.
- [90] H.H. Teng, P. Fenter, L. Cheng, N.C. Sturchio, Resolving orthoclase dissolution processes with atomic force microscopy and X-ray reflectivity, *Geochim. Cosmochim. Acta.* 65 (2001) 3459–3474. doi:10.1016/S0016-7037(01)00665-2.
- [91] G. Jordan, S.R. Higgins, C.M. Eggleston, S.M. Swapp, D.E. Janney, K.G. Knauss, Acidic dissolution of plagioclase: in-situ observations by hydrothermal atomic force microscopy, *Geochim. Cosmochim. Acta.* 63 (1999) 3183–3191. doi:10.1016/S0016-7037(99)00225-2.
- [92] T.C. Labotka, D.R. Cole, M. Fayek, L.R. Riciputi, F.J. Stadermann, Coupled cation and oxygen-isotope exchange between alkali feldspar and aqueous chloride solution, *Am. Mineral.* 89 (2004) 1822–1825. doi:10.2138/am-2004-11-1229.
- [93] E. Pustovgar, R.P. Sangodkar, A.S. Andreev, M. Palacios, B.F. Chmelka, R.J. Flatt, J.-B. d’Espinoze de Lacaille, Understanding silicate hydration from quantitative analyses of hydrating tricalcium silicates, *Nat. Commun.* 7 (2016) 10952. doi:10.1038/ncomms10952.
- [94] M.C. Ball, R.E. Simmons, I. Sutherland, Surface composition of anhydrous portland cements, *Cem. Concr. Res.* 18 (1988) 29–34. doi:10.1016/0008-8846(88)90118-4.
- [95] W. Gerhard, E. Nägele, The hydration of cement studied by secondary ion mass spectrometry (SIMS), *Cem. Concr. Res.* 13 (1983) 849–859. doi:10.1016/0008-8846(83)90086-8.
- [96] S.S.S. Rajan, Sulfate adsorbed on hydrous alumina, ligands displaced, and changes in surface charge, *Soil Sci. Soc. Am. J.* 42 (1978) 39–44. doi:10.2136/sssaj1978.03615995004200010009x.
- [97] L.E. Davidson, S. Shaw, L.G. Benning, The kinetics and mechanisms of schwertmannite transformation to goethite and hematite under alkaline conditions, *Am. Mineral.* 93 (2008) 1326–1337. doi:10.2138/am.2008.2761.
- [98] X. Lin, R.C. Burns, G.A. Lawrance, Effect of cadmium(II) and anion type on the ageing of ferrihydrite and its subsequent leaching under neutral and alkaline conditions, *Water. Air. Soil Pollut.* 143 (2003) 155–177. doi:10.1023/A:1022850308363.
- [99] R.L. Parfitt, R.S.C. Smart, The mechanism of sulfate adsorption on iron oxides, *Soil Sci. Soc. Am. J.* 42 (1978) 48–50. doi:10.2136/sssaj1978.03615995004200010011x.
- [100] G. Åkerlöf, Dielectric constants of some organic solvent-water mixtures at various temperatures, *J. Am. Chem. Soc.* 54 (1932) 4125–4139. doi:10.1021/ja01350a001.

## SUPPLEMENTARY INFORMATION: APPENDIX

### *A.1 In situ XRD Configuration*

Figure A.1 shows an image of the experimental configuration for the *in situ* XRD. A syringe injection pump metered a known volume of solution for a 1:1 solution-to- $C_3A$  (by mass) experiment. Figure A.2 shows a detail of the sample configuration. A small amount (16 mg to 18 mg) of  $C_3A$  sat on top of a glass wool pack, such that only the powder was exposed to the solution for the duration of the experiment.

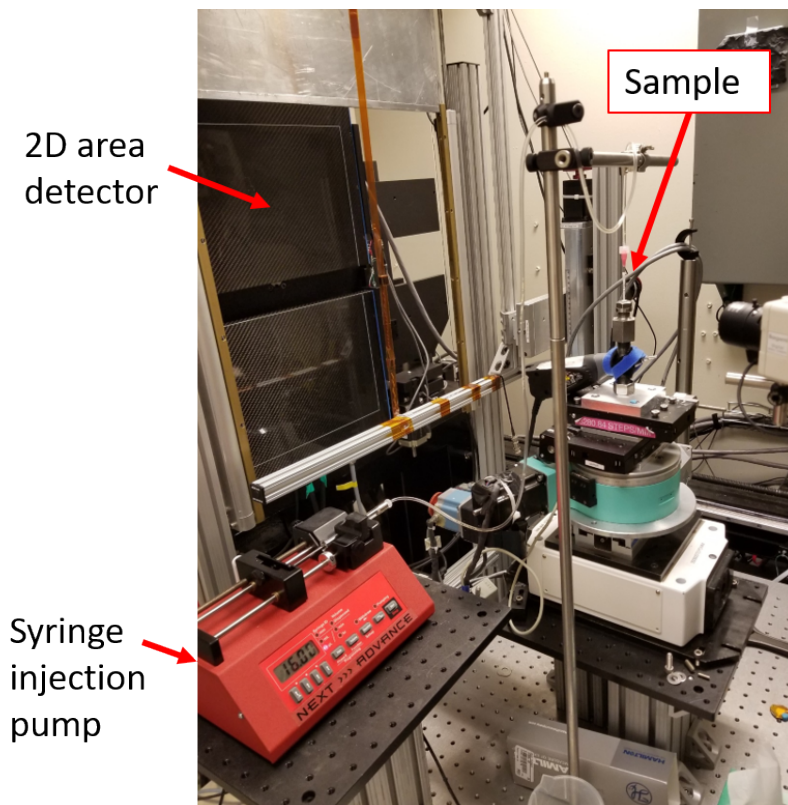


Figure A.1. *In situ* XRD configuration.

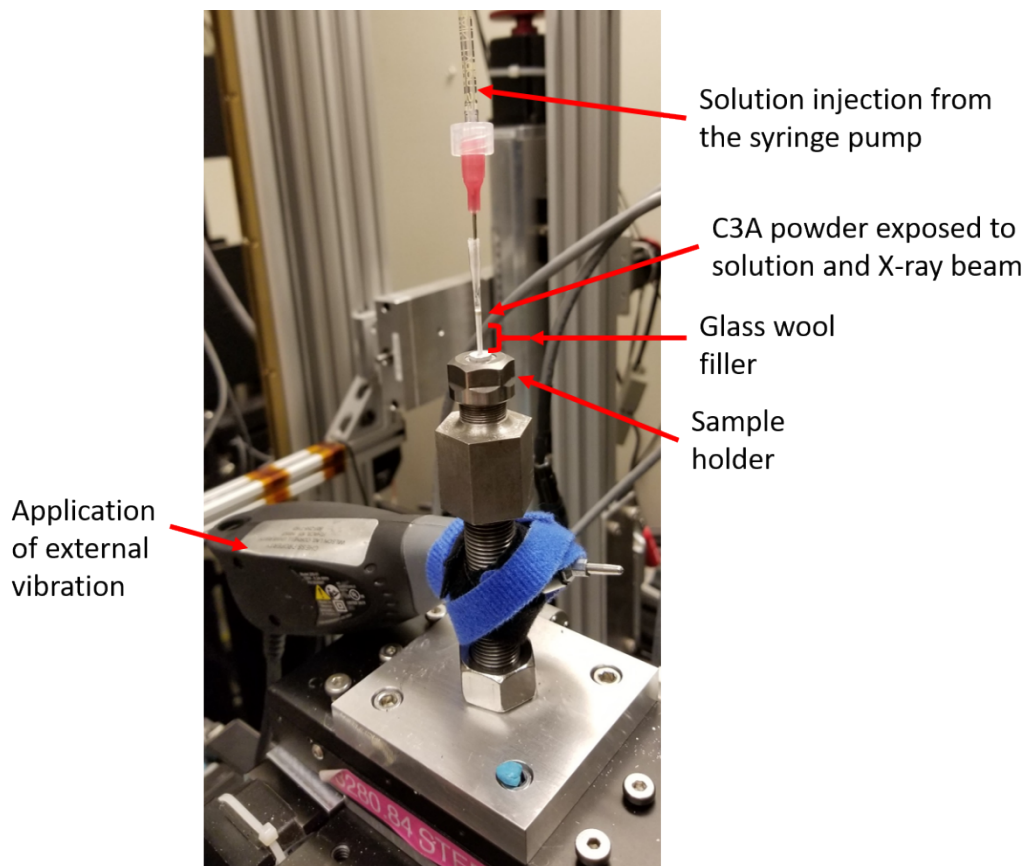


Figure A.2. Sample configuration for *in situ* XRD experiments.

### A.2 Additional TOF-SIMS Data and Figures

Figure A.3 shows the Ca/Al intensity ratios obtained at replicate locations. For the control (Figure A.3a), the two replicate locations showed approximately similar trends, so the average of the two locations was used in Section 3.2 (*e.g.*, Figure 6). Similar to the control sample, the same trends were observed for the replicate locations from the  $K_2SO_4$  (Figure A.3d) and  $Na_2SO_4$  (Figure A.3e) exposed samples, which is why the average of those were also presented in Section 3.2. For the water exposed sample (Figure A.3b), Location 1 presented a different trend compared to the same trend observed at Locations 2 and 3; therefore, the trend from Location 1 and the average of Locations 2 and 3 were used in Section 3.2. Finally, the  $MgSO_4$  exposed sample presented similar but slightly different trends at the two locations, so both were included in Section 3.2.

Figure A.4 shows the elemental profiles as intensity counts *vs.* sputter time. These data were used to create the additional figures in Section 3.2. The data are only shown up until a sputter time of 4000 s in Figure A.4, since the data were relatively constant after then and since the key trends to observe were mostly within the first about 1000 s of sputter time. While additional ions and ion complexes were observable by TOF-SIMS (*e.g.*,  $H^+$ ,  $CaO^+$ ,  $CaOH^+$ ,  $C^+$ ,  $CaH^+$ ,  $^{44}Ca^+$ ,  $Cs_2O^+$ ), only the profiles directly relevant to the discussion in Section 3.2 are included in Figure A.4.

Sputter depth calibration was performed on a 200  $\mu\text{m}$  by 200  $\mu\text{m}$  crater for the sample exposed to  $\text{MgSO}_4$  solution. An atomic force microscopy (AFM) probe was used to measure the relative crater depth at approximately the same location after 0 s, 500 s, 1000 s, 1500 s, 3000 s, and 6000 s of sputtering (Figure A.5). Surface topography is evident in Figure A.5, particularly pores, so the sputter-depth calibration was conducted from a number of locations that appeared to be free from such texture; these locations are identified by boxes in Figure A.5 and shown in Figure A.6.

The data in Figure A.6 represents 1922 sputter depth measurements. Referencing the relative height before any sputtering as zero, the relative mean and standard deviation depth of sputtering after 500 s, 1000 s, 1500 s, 3000 s, and 6000 s are -33.4 nm and 6.2 nm, -39.6 nm and 6.7 nm, -59.0 nm and 6.3 nm, -85.8 nm and 7.9 nm, and -141.6 nm and 6.8 nm, respectively (Figure A.7). The crater depth as a function of sputter time appears to follow a bilinear behavior, with a faster material removal rate from 0 s to 500 s and a slower rate from 500 s to 6000 s. This behavior may be expected, given that there is a lower Ca/Al ratio near the surface compared to the bulk material (Figure A.3). Indeed this behavior appears to be true for the mean values as well as at individual locations in the sputtered crater (Figure A.8). Assuming this bilinear relationship, the mean, median, and standard deviation of the sputter rate from 0 s to 500 s is -0.067  $\text{nm s}^{-1}$ , -0.066  $\text{nm s}^{-1}$ , and 0.013  $\text{nm s}^{-1}$ , respectively, and the mean, median, and standard deviation of the sputter rate from 500 s to 6000 s is -0.020  $\text{nm s}^{-1}$ , -0.020  $\text{nm s}^{-1}$ , and < 0.001  $\text{nm s}^{-1}$ , respectively (Table A.1). Thus, there is apparently greater variability in the initial surface sputter rate (Table A.1 and Figure A.9), possibly due to the spatial variation in Ca/Al (and other) ratios, while the bulk material has a very consistent sputter rate as the material composition is more uniform.

The signal intensities for the  $\text{Cs}_2\text{S}^+$  and  $\text{CsS}^+$  ion complexes are shown relative to the Al intensity in Figure A.10. Only one location is shown for each sulfate salt, since the behavior was similar between both locations. The  $\text{Cs}_2\text{S}/\text{Al}$  ratio is significantly greater than the  $\text{CsS}/\text{Al}$  ratio for the  $\text{MgSO}_4$  and the  $\text{Na}_2\text{SO}_4$  samples, whereas the reverse is true for the  $\text{K}_2\text{SO}_4$  samples.

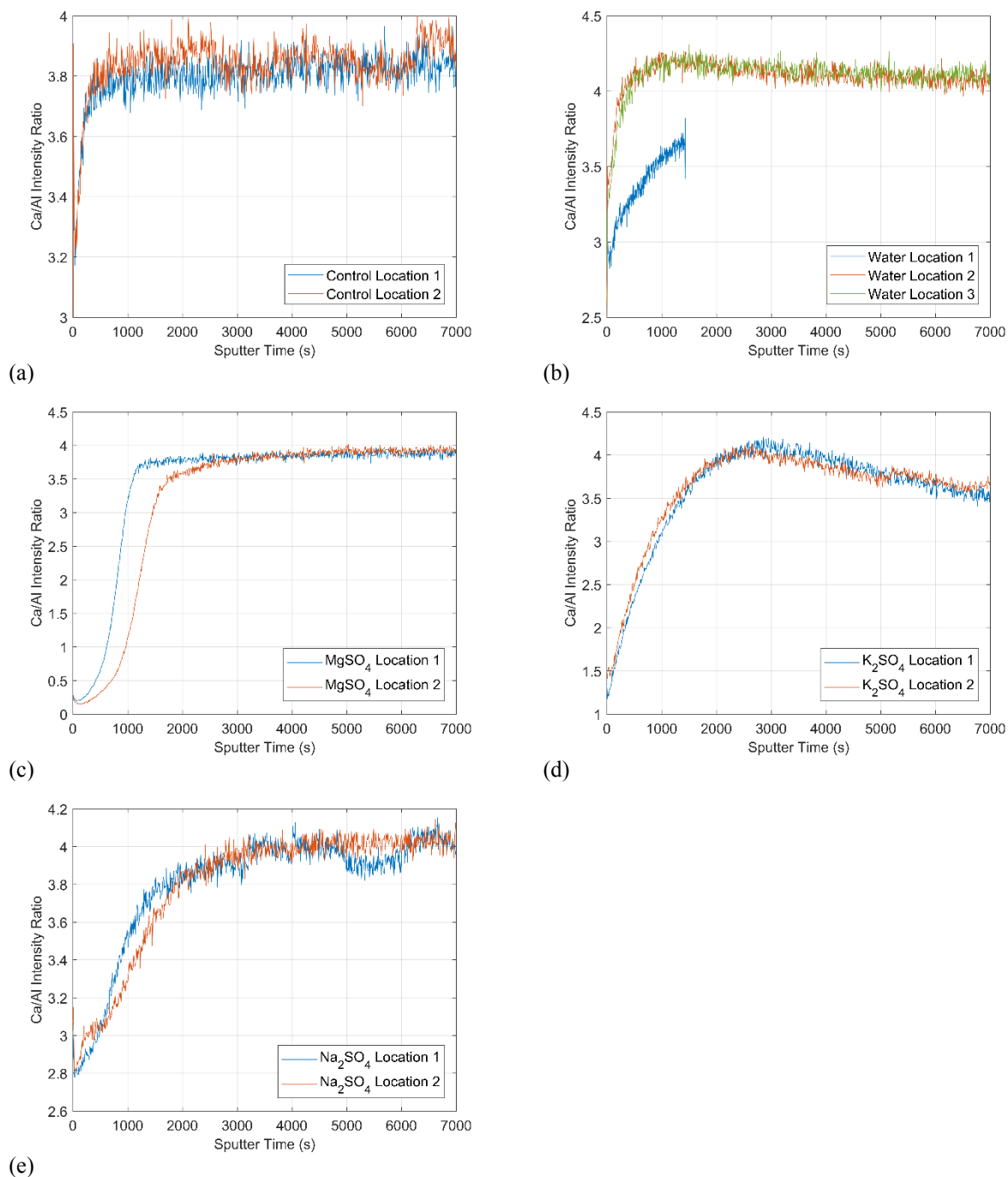


Figure A.3. Ca/Al intensity ratios for each of the replicate locations tested by TOF-SIMS, including (a) the control sample and samples exposed to (b) 40 % deionized water and 60 % ethanol, (c) 40 % deionized water and 60 % ethanol with 1 mmol L<sup>-1</sup> MgSO<sub>4</sub>, (d) 40 % deionized water and 60 % ethanol with 1 mmol L<sup>-1</sup> K<sub>2</sub>SO<sub>4</sub>, and (e) 40 % deionized water and 60 % ethanol with 1 mmol L<sup>-1</sup> Na<sub>2</sub>SO<sub>4</sub>.

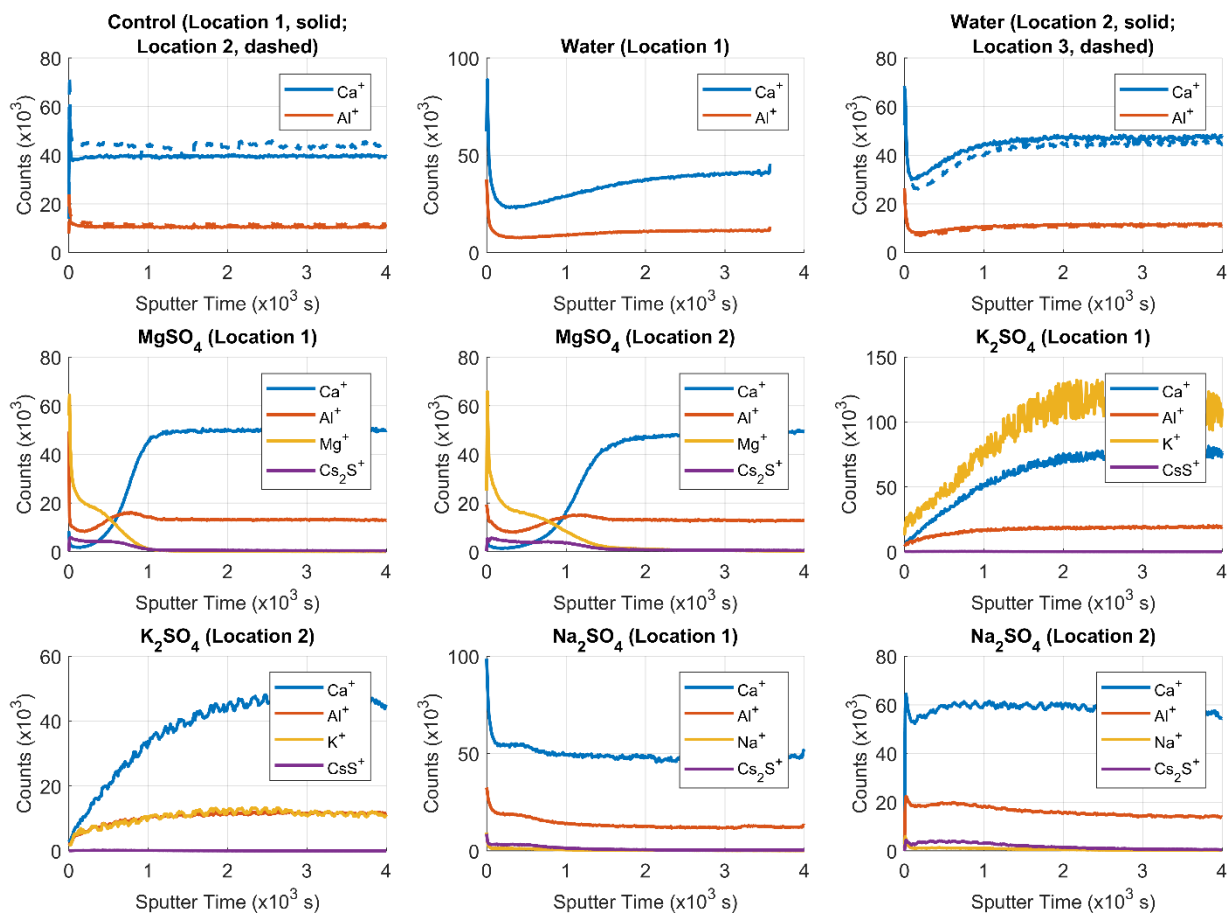


Figure A.4. Relevant elemental profiles from each TOF-SIMS specimen. Note: data are only shown up until a sputter time of 4000 s, since the data were relatively constant after then.

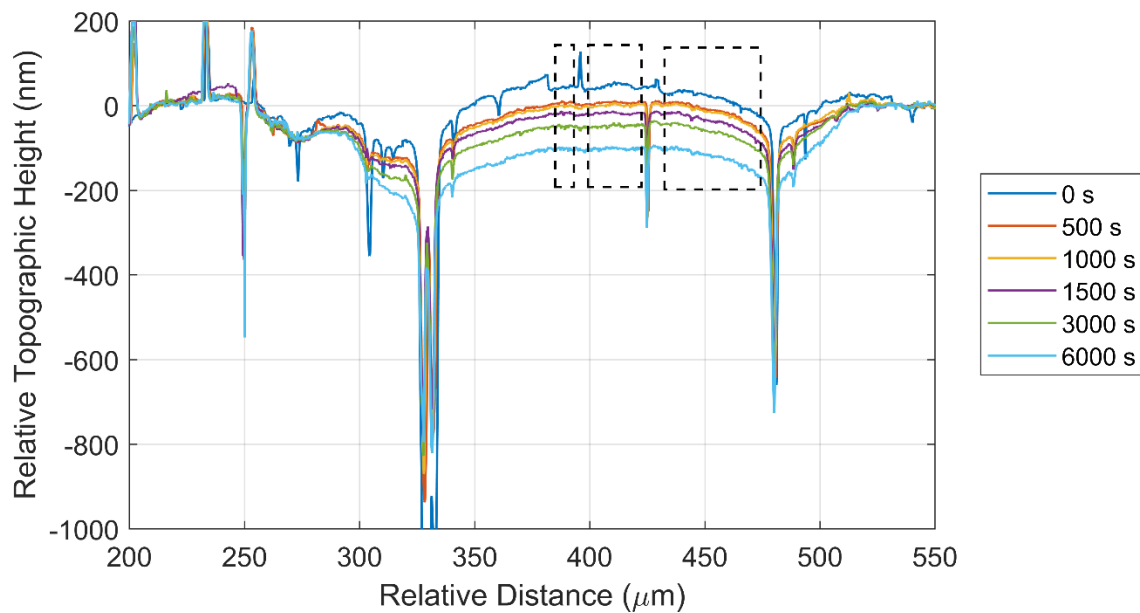


Figure A.5. Sputter-depth calibration plot, showing the AFM data windowed on the 200- $\mu\text{m}$  sputtered crater. The dashed-line boxes indicate the approximate regions that sputter-depth calibration was performed.

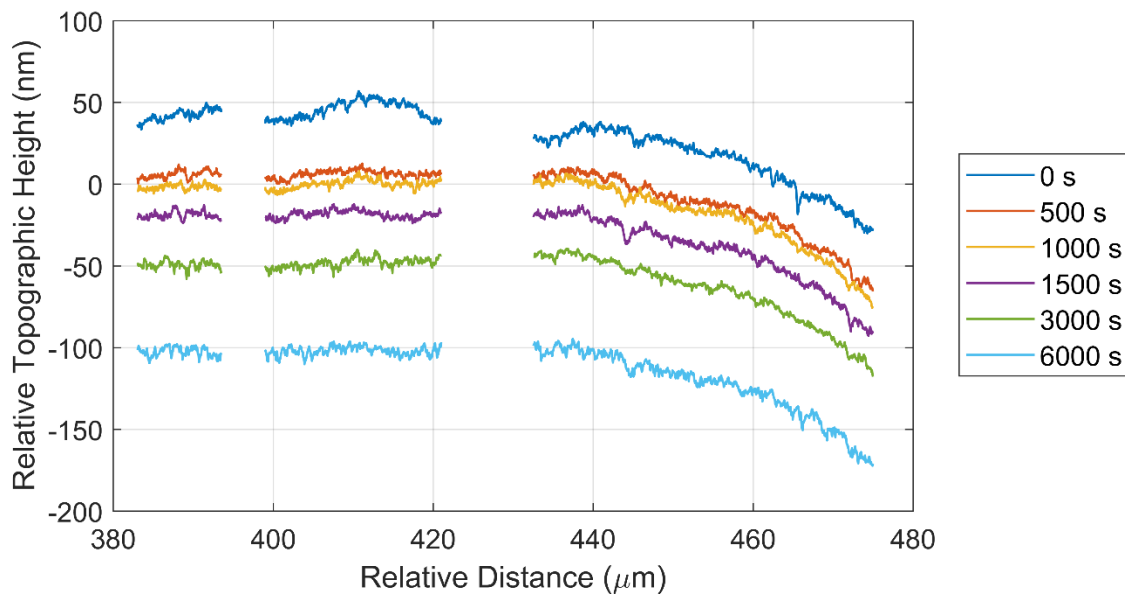


Figure A.6. Sputter-depth calibration plot, showing the boxed regions from Figure A.5.

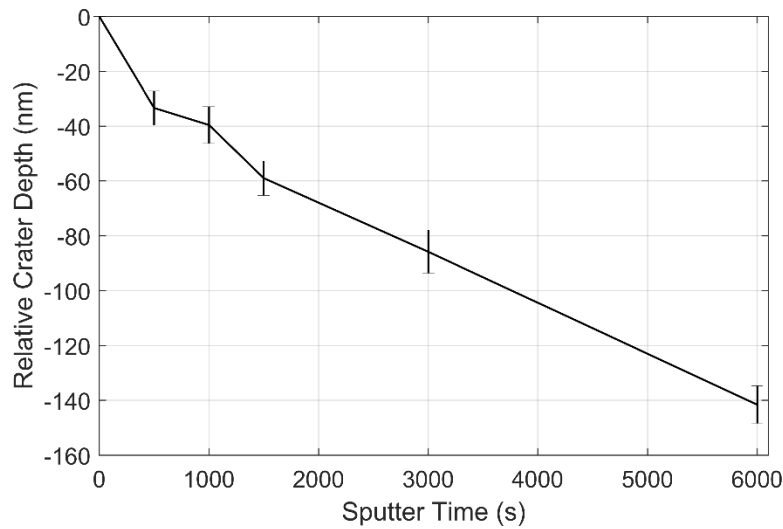


Figure A.7. Mean and standard deviation of the relative crater depth as a function of sputter time from the 1922 locations in Figure A.6.

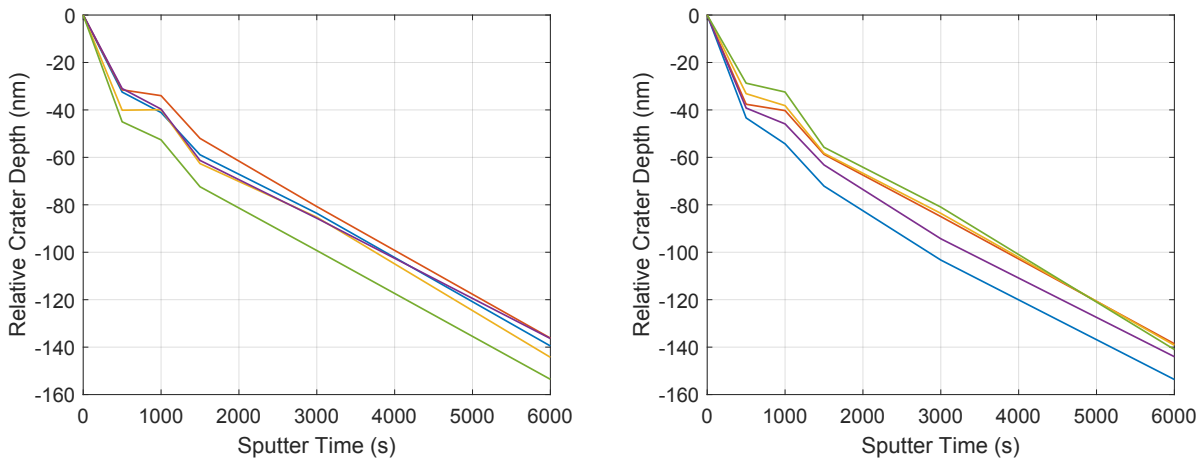


Figure A.8. Relative crater depth vs. sputter time at five (left) and five other (right) randomly-selected locations within the crater. Line color represents different locations and are unrelated between the two figures.

Table A.1. Statistics of the Bilinear Sputter Rates ( $\text{nm s}^{-1}$ )

	Sputter rate from 0 s to 500 s	Sputter rate from 500 s to 6000 s
Mean	-0.0667	-0.0198
Median	-0.0664	-0.0198
Standard deviation	0.0125	0.0005
Interquartile range (IQR)*	0.0151 (-0.0742, -0.0591)	0.0007 (-0.0201, -0.0194)

\*Data presented as: IQR (25<sup>th</sup> percentile, 75<sup>th</sup> percentile)

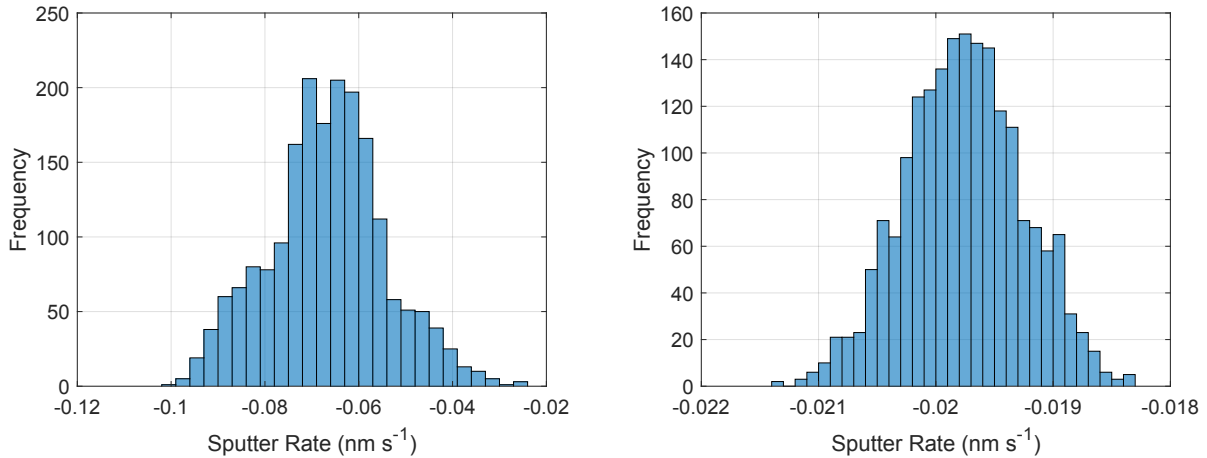


Figure A.9. Histograms of the bilinear sputter rates determined from the 1922 locations in Figure A.5: sputter rate from 0 s to 500 s (left) and from 500 s to 6000 s (right). Statistics of these distributions are shown in Table A.1.

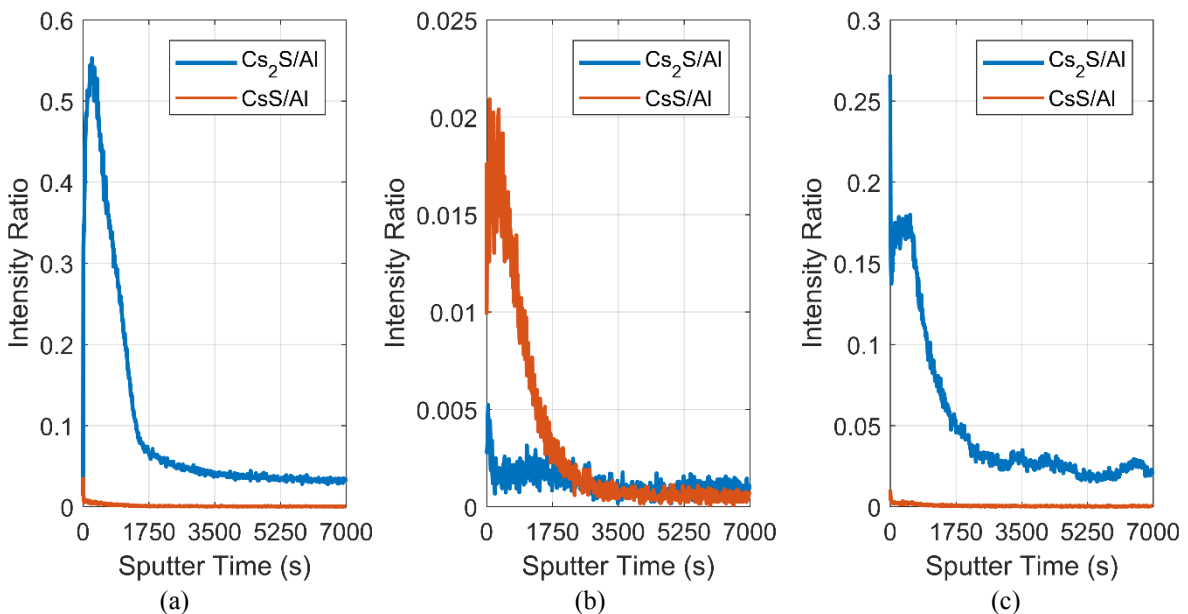


Figure A.10.  $\text{Cs}_2\text{S}/\text{Al}$  and  $\text{CsS}/\text{Al}$  intensity ratios for (a)  $\text{MgSO}_4$  (Location 2), (b)  $\text{K}_2\text{SO}_4$  (Location 2), and (c)  $\text{Na}_2\text{SO}_4$  (Location 2).

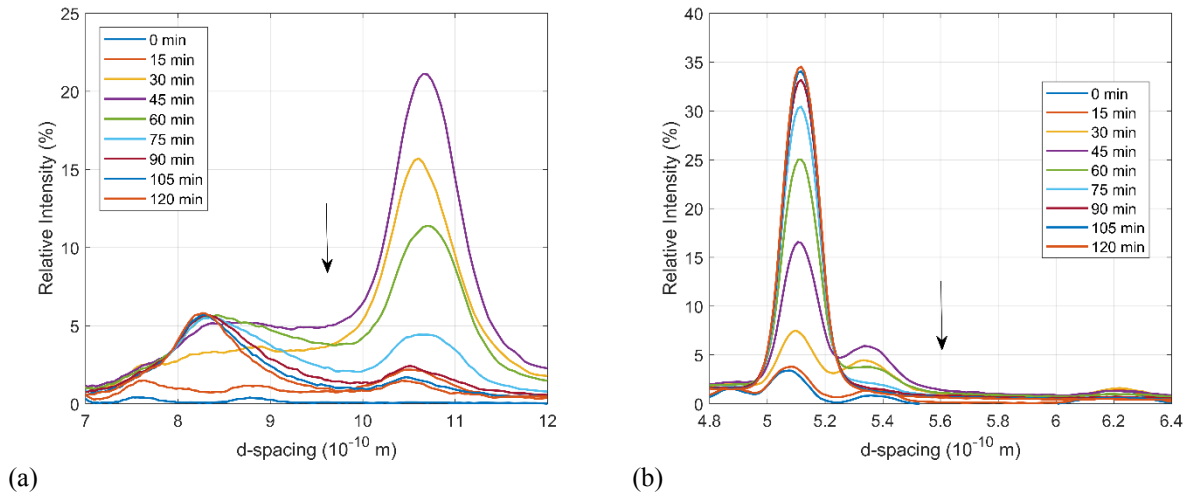
### A.3 Additional XRD Data and Figures

Figure A.11 shows the same data as Figure 12, windowed to instead show the locations for potential ettringite peaks at 0.972 nm (9.72 Å) and 0.561 nm (5.61 Å) (PDF 41-1451). As Figure A.11 demonstrates, no peaks for ettringite were identified, further confirming that the phase was not present.

Figure A.12 shows the XRD patterns from Figure 10a between 0 min and 30 min, particularly showing the peaks between 0.7 nm (7 Å) and 1.2 nm (12 Å). Certainly the main peak for  $\text{C}_4\text{AH}_{19}$  is present at around 1.07 nm (10.7 Å). However, similar to what was demonstrated

for the sulfate solution experiments (*e.g.*, Figure 12 and Figure A.11), there is also a shoulder peak extending from around 0.8 nm (8 Å) to 1.0 nm (10 Å), which is suspected to be a solid solution of AFm-type phases. For the deionized water experiment in Figure A.12, this solid solution is suspected to be attributable to hydroxy and carbonate (*e.g.*, hemcarbonate) AFm phases.

Figure A.13 shows the time-dependent relative phase intensities of  $C_3A$ ,  $C_4AH_{19}$ , hydrogarnet, and AFm solid solution for the hydration experiments with deionized water and sulfate solution. The data in Figure A.13 was used to populate Table 6.



(a) Figure A.11. Data from Figure 12 ( $10 \text{ mmol L}^{-1}$   $\text{CaSO}_4$  solution) windowed to show (black arrows) where the anticipated main peaks for ettringite would appear at (a) 0.972 nm (9.72 Å) and (b) 0.561 nm (5.61 Å).

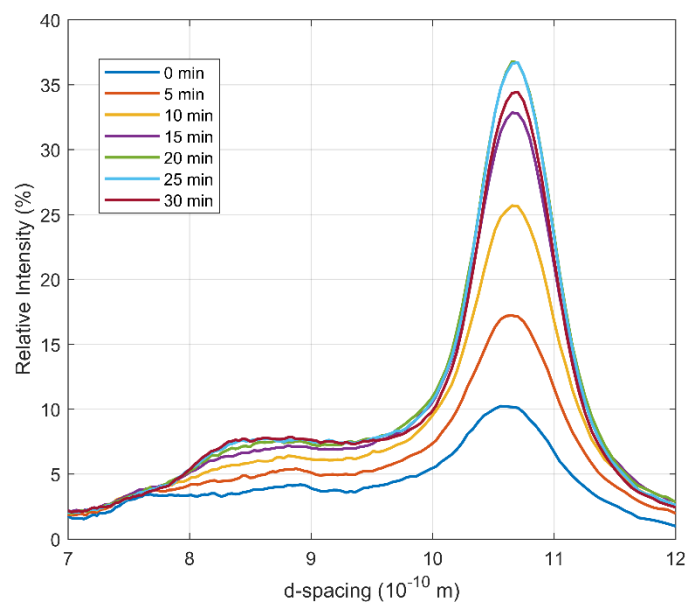


Figure A.12. Time dependent XRD data from Figure 10a (deionized water) windowed to show the peaks present between 0.7 nm (7 Å) and 1.2 nm (12 Å).

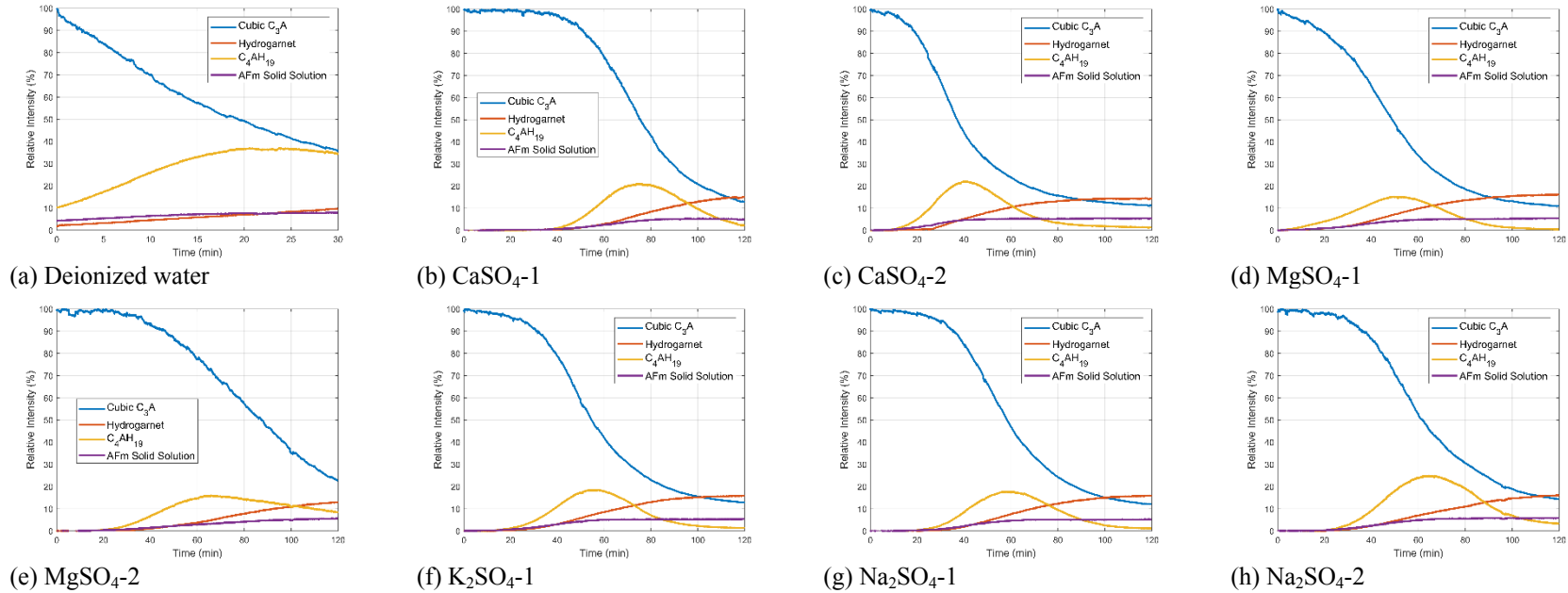


Figure A.13. Relative intensities for each phase from C<sub>3</sub>A hydration with solutions in (a) deionized water and 10 mmol L<sup>-1</sup> solutions of (b,c) CaSO<sub>4</sub>, (d,e) MgSO<sub>4</sub>, (f) K<sub>2</sub>SO<sub>4</sub>, and (g,h) Na<sub>2</sub>SO<sub>4</sub>.